PBRM1 Deficiency Confers Synthetic Lethality to DNA Repair Inhibitors in Cancer

Roman M Chabanon, Daphné Morel, Thomas Eychenne, Léo Colmet-Daage, Ilirjana Bajrami, Nicolas Dorvault, Marlène Garrido, Cornelia Meisenberg, Andrew Lamb, Carine Ngo, et al.

PBRM1 deficiency confers synthetic lethality to DNA repair inhibitors in cancer

Roman M Chabanon[1,2,*] & Daphné Morel[1,3,*], Thomas Eychenne[1], Léo Colmet-Daage[1], Ilirjana Bajrami[2], Nicolas Dorvault[1], Marlène Garrido[1], Cornelia Meisenberg[4], Andrew Lamb[5], Carine Ngo[1], Suzanna R Hopkins[4], Theodoros I Roumeliotis[6], Samuel Jouny[2], Clémence Hénon[1], Asuka Kawai-Kawachi[1], Clémence Astier[1], Asha Konde[2], Elaine Del Nery[7], Christophe Massard[8], Stephen J Pettitt[2], Raphaël Margueron[9], Jyoti S Choudhary[6], Geneviève Almouzni[10,11], Jean-Charles Soria[3], Eric Deutsch[3,12], Jessica A Downs[4], Christopher J Lord[2,**], Sophie Postel-Vinay[1,3,8,**]

[1]ATIP-Avenir group, Inserm Unit U981, Gustave Roussy, Villejuif, France; [2]The CRUK Gene Function Laboratory and Breast Cancer Now Toby Robins Breast Cancer Research Centre, The Institute of Cancer Research, London, United Kingdom; [3]Université Paris Saclay, Université Paris-Sud, Faculté de Médicine, Le Kremlin Bicêtre, France; [4]Epigenetics and Genome Stability Team, The Institute of Cancer Research, London, United Kingdom; [5]Sage Bionetworks, Seattle, USA; [6]Functional Proteomics Team, The Institute of Cancer Research, London, United Kingdom; [7]Institut Curie, PSL Research University, Department of Translational Research, The Biophenics High-Content Screening Laboratory, Cell and Tissue Imaging Facility (PICT-IBiSA), 75005, Paris, France. [8]Drug Development Department, DITEP, Gustave Roussy, Villejuif, France. [9]Institut Curie, PSL Research University, INSERM Unit U934, CNRS UMR 3215, 75005, Paris, France. [10]Institut Curie, PSL Research University, CNRS, UMR 3664, Equipe Labellisée Ligue contre le Cancer, 75005, Paris, France; [11]Sorbonne Universités, UPMC Université Paris-VI, CNRS, UMR3664, 75005, Paris, France; [12]INSERM UMR1030 Molecular Radiotherapy and Therapeutic Innovations, Gustave Roussy, Villejuif, France.

Running title. PBRM1/DNA repair inhibitors synthetic lethality.

Keywords. PARP inhibitors, ATR inhibitors, PBRM1 deficiency, synthetic lethality, cGAS/STING, R-loop.

*** Joint first authorship; ** Corresponding authors;**

	Sophie Postel-Vinay	**Christopher Lord**
Mail	114 rue Edouard Vaillant 94800 Villejuif, France	237 Fulham Road SW3 6JB London, UK
Email	sophie.postel-vinay@gustaveroussy.fr	chris.lord@icr.ac.uk
Phone	+33(0)142114343	+44(0)2071535000

Conflict of Interest and Financial Disclosure. Authors have no conflicts of interest or financial interests to disclose. SPV has received research funding from Merck KGaA, Boehringer Ingelheim and Roche for unrelated research projects. As part of the Drug Development Department (DITEP), SPV is principal investigator or sub-investigator of clinical trials from Abbvie, Agios Pharmaceuticals, Amgen, Argen-X Bvba, Arno Therapeutics, Astex Pharmaceuticals, Astra Zeneca, Aveo, Bayer Healthcare Ag, Bbb Technologies Bv, Blueprint Medicines, Boehringer Ingelheim, Bristol Myers Squibb, Celgene Corporation, Chugai Pharmaceutical Co., Clovis Oncology, Daiichi Sankyo, Debiopharm S.A., Eisai, Eli Lilly, Exelixis, Forma, Gamamabs, Genentech, Inc., Glaxosmithkline, H3 Biomedicine, Inc, Hoffmann La Roche Ag, Innate Pharma, Iris Servier, Janssen Cilag, Kyowa Kirin Pharm. Dev., Inc., Loxo Oncology, Lytix Biopharma As, Medimmune, Menarini Ricerche, Merck Sharp & Dohme Chibret, Merrimack Pharmaceuticals, Merus, Millennium Pharmaceuticals, Nanobiotix, Nektar Therapeutics, Novartis Pharma, Octimet Oncology Nv, Oncoethix, Onyx Therapeutics, Orion Pharma, Oryzon Genomics, Pfizer, Pharma Mar, Pierre Fabre, Roche, Sanofi Aventis, Taiho Pharma, Tesaro Inc, and Xencor. SPV has participated to advisory boards for Merck KGaA. CJL is a named inventor on patents describing the use of DNA repair inhibitors and stands to gain from their use as part of the Institute of Cancer Research “Rewards to Inventor” scheme. CJL has received research funding from Astra Zeneca, Merck KGaA, Artios, Pfizer and has received consultancy and/or advisory fees from Artios, Astra Zeneca, MerckKGaA, Tango, and GLG. CJL is a shareholder of OviBio and Tango. JCS was a full-time employee of Medimmune/Astra Zeneca from September 2017 to December 2019. JCS has received consultancy fees from AstraZeneca, Astex, Clovis, GSK, GamaMabs, Lilly, MSD, Mission Therapeutics, Merus, Pfizer, PharmaMar, Pierre Fabre, Roche-Genentech, Sanofi, Servier, Symphogen, and Takeda. JCS is a shareholder of Gritstone. ED has received consultancy fees from Roche, Astra Zeneca, MSD, AMGEN, Accuray, and Boehringer.

Main text = 5540 words

6 Figures, 20 Supp. Figures

7 Supp. Tables

4 Supp. Videos

Abstract

Inactivation of *Polybromo 1* (*PBRM1*), a specific subunit of the PBAF chromatin remodeling complex, occurs frequently in cancer, including 40% of clear cell renal cell carcinomas (ccRCC). To identify novel therapeutic approaches to targeting PBRM1-defective cancers, we used a series of orthogonal functional genomic screens which identified PARP and ATR inhibitors as being synthetic lethal with *PBRM1* deficiency. The PBRM1/PARP inhibitor synthetic lethality was recapitulated using several clinical PARP inhibitors in a series of *in vitro* model systems, and *in vivo* in a xenograft model of ccRCC. In the absence of exogenous DNA damage, PBRM1-defective cells exhibited elevated levels of replication stress, micronuclei, and R-loops. PARP inhibitor exposure exacerbated these phenotypes. Quantitative mass spectrometry revealed that multiple R-loop processing factors were downregulated in PBRM1-defective tumor cells. Exogenous expression of the R-loop resolution enzyme RNase H1 reversed the sensitivity of PBRM1-deficient cells to PARP inhibitors, suggesting that excessive levels of R-loops could be a cause of this synthetic lethality. PARP and ATR inhibitors also induced cyclic GMP-AMP synthase/stimulator of interferon genes (cGAS/STING) innate immune signaling in PBRM1-defective tumor cells. Overall, these findings provide the preclinical basis for using PARP inhibitors in PBRM1-defective cancers.

Significance: This study demonstrates that PARP and ATR inhibitors are synthetic lethal with the loss of PBRM1, a PBAF-specific subunit, thus providing the rationale for assessing these inhibitors in patients with PBRM1-defective cancer.

Introduction

Polybromo 1 (PBRM1), a tumor suppressor gene encoding the BAF180 protein, is a specific subunit of the polybromo-associated BAF (PBAF) complex, which is one of the three classes of SWItch/Sucrose Non-Fermentable (SWI/SNF) chromatin remodeling complexes (1). PBRM1 contains six bromodomains, which recognize acetylated lysine histone residues (2–4), and is involved in preserving genome and chromosomal stability by maintaining centromeric cohesion during mitosis (5). During interphase, PBRM1 also facilitates replication re-priming downstream of stalled replication forks (6) and promotes DNA repair by mediating transcriptional silencing at DNA double-strand breaks (DSBs), via ATM- (7) and cohesin-dependent processes (8). Additionally, PBRM1 influences the anti-tumor immune response (9), notably by mediating resistance to T-cell-dependent killing in preclinical cancer models (10).

PBRM1 is one of the most frequently altered genes in cancer. Deleterious *PBRM1* mutations are found in 28-55% of clear cell renal cell carcinomas (ccRCC), where they are an early, driver event (11) that occurs subsequent to *VHL* alteration. When evaluated by immunohistochemistry, loss of PBRM1 expression is seen in 57-84% of ccRCC, particularly in advanced disease (12–15). Several other aggressive malignancies also harbor PBRM1 defects, including 11-59 % of chordomas, 12-23 % of cholangiocarcinomas, 7-20 % of mesotheliomas, 12 % of endometrial carcinomas, and 3% of non-small cell lung cancers (NSCLC) (16–18).

There are currently no personalized medicine approaches that target PBRM1-defective cancers, an area of unmet medical need (19,20). We show here that clinical Poly-(ADP)-Ribose Polymerase inhibitors (PARPi) cause synthetic lethality

(SL) with PBRM1 defects, thereby representing a novel, readily-testable, precision medicine-based therapeutic strategy for PBRM1-defective cancers.

Materials and Methods

Cell lines

U2OS, H1299, A549, RCC-MF and RCC-FG2 cell lines were purchased from ATCC. 786-O and A498 cell lines were kindly provided by Dr. Sophie Gad-Lapiteau. HAP1 *PBRM1*-isogenic cells were purchased from Horizon Discovery. U2OS, A549, A498 cells were cultured in high-glucose Dulbecco's Modified Eagle Medium (DMEM) supplemented with 10% fetal bovine serum (FBS). H1299 and 786-O cells were cultured in Roswell Park Memorial Institute-1640 (RPMI-1640) medium supplemented with 10% FBS. RCC-MF and RCC-FG2 cells were cultured in RPMI-1640 medium supplemented with 2 mM L-glutamine and 10% FBS (and 4.5 g/L glucose for RCC-MF). HAP1 cells were cultured in Iscove's Modified Dulbecco's Medium (IMDM) supplemented with 10% FBS. All cells were grown at 37°C and 5% CO_2. Mycoplasma testing was performed monthly using the MycoAlert Mycoplasma Detection Kit (Lonza). All cell lines were short-tandem-repeat typed using StemElite ID (Promega) to confirm identity. Further details on cell lines, including their histological and genetic backgrounds, as well as technical information on their use in the study are shown in Supplementary Tables S1 and S2.

Drugs and chemicals

The PARP inhibitors olaparib (AZD-2281), rucaparib (PF-01367338), and talazoparib (BMN-673), and the ATR inhibitors berzosertib (VE-822) and ceralasertib (AZD6738) were purchased from Selleck Chemicals. Inhibitor stock solutions were prepared in dimethyl sulfoxide (DMSO) and stored in aliquots at -80°C. Mitomycin C (MMC), 5,6-

dichlorobenzimidazole 1-β-D-ribofuranoside (DRB), iodo-deoxyuridine (IdU), and 5-chloro-2′-deoxyuridine (CldU) were obtained from Sigma-Aldrich. PicoGreen® was purchased from ThermoFisher.

CRISPR/Cas9 targeting for the generation of *PBRM1*-KO cell lines

PBRM1 gene knockout was performed in U2OS, 786-O, A498, H1299 and A549 cell lines using a CRISPR/Cas9-based gene editing approach. Cells were targeted using the Edit-R™ CRISPR/Cas9 gene engineering protocol (Horizon), according to the supplier's instructions. The 5′-TTCATCCTTATAGTCTCGGA-3′ sgRNA sequence was used to generate a frameshift deletion in exon 3 of *PBRM1*. Cells were transfected in T25 flasks with sgRNA and Cas9 plasmid, using Lipofectamine 2000 (Thermo Fisher). Several rounds of transfection were performed to obtain optimal knockout efficiency. PBRM1 expression was monitored in the transfected pool at each transfection cycle by western blot. Once expression was no longer detected, cells were plated onto 96-well plates for clonal isolation using the limiting dilution method. Colonies were recovered and profiled for PBRM1 expression by western blot.

Small-molecule and siRNA synthetic lethal screens

Small-molecule and siRNA screens were performed as described previously (21). The small-molecule inhibitors and siRNA targets used in these screens are listed in Supplementary Tables S3-5. See also Supplementary Materials and Methods for further details.

Cell-based assays

Cell survival assays were conducted as previously described (21). See also Supplementary Materials and Methods for details.

DNA combing

Cells were grown in 10 cm dishes and exposed to 10 µM olaparib or DMSO for 48 h to reach 70% confluence at the time of harvesting. For replication forks labeling, cells received pre-warmed medium containing 100 µM CldU and were incubated at 37^{o}C, 5% CO_2 for 30 min. Cells were then rinsed 3 times with pre-chilled PBS and incubated with 100 µM IdU for 30 min. Cells were collected in cold PBS, counted and adjusted to 50,000 cells per 50 µL PBS on ice. Plugs were generated by adding 50 µL of pre-warmed 1% law-melting point agarose to the cells; the resulting 100 µL mix was gently homogenized and quickly transferred into a casting mold, and incubated for 1 hr at 4°C to solidify. Subsequent steps were performed as previously described (22). For the analysis, initiation, termination and cluster patterns of replicative forks were considered to measure fork velocity.

Immunofluorescence and image analysis

For quantification of γH2AX, RAD51, RPA foci and micronuclei, cells were seeded in 96-well plates (Greiner Bio-One #655090) and treated with the indicated drugs. Cells were then fixed in 4% paraformaldehyde for 20 min at RT, washed twice with PBS, and permeabilized with 0.2% Triton X-100 in PBS for 10 min. Subsequent labeling, imaging and image analysis steps were performed as previously described (23).

***In vivo* experiment**

Animal experimentation was carried out according to ARRIVE guidelines, regulations set out in the UK Animals (Scientific Procedures) Act 1986, and in line with a UK Home Office project license held by CJL and approved by the ICR Animal Welfare and Ethical Review Body (AWERB). 786-O *PBRM1*-WT or -KO chunks (between 1x1 mm and 2x2 mm) were subcutaneously implanted into the flank of 5-weeks-old

female NOD.Cg-Prkdc^{scid} Il2rg^{tm1Wjl}/SzJ mice, with a take rate of 87%. When the tumor reached the 40-50 mm^3 threshold size, mice were randomized into vehicle (control) or treatment groups (*PBRM1*-WT: N=11 vehicle, N=11 talazoparib; *PBRM1*-KO: N=10 vehicle, N=9 talazoparib). Mice received 0.25 mg/kg talazoparib or vehicle daily for 6 weeks *per os*. Tumor size was monitored twice weekly during four weeks using calipers.

Statistical analyses

Apart from the *in vivo* experiment, no statistical methods were used to predetermine sample size and experiments were not randomized. The investigators were not blinded during xenograft experiments. Unless otherwise stated, all graphs show mean values with error bars (standard deviation, SD); 95% confidence intervals were used and significance was considered when * $P < 0.05$, ** $P < 0.01$, *** $P < 0.001$, **** $P < 0.0001$; ns, not significant.

Data availability

The proteomics and DRIP-Seq datasets are publicly available at Pride (http://www.ebi.ac.uk/pride) under the accession number PXD017826, and at Array Express (https://www.ebi.ac.uk/arrayexpress/), under the accession number E-MTAB-8837, respectively.

Additional methods details are available in Supplementary Materials and Methods. All uncropped and unedited images of the blots included in this study are available in Figure S20.

Results

Orthogonal genetic and small-molecule inhibitor screens identify PBRM1/PARP inhibitor synthetic lethal effects

To uncover clinically actionable vulnerabilities associated with PBRM1 deficiency, we performed three orthogonal drug sensitivity and/or genetic perturbation screens (Fig. 1, Fig. S1A-F). First, we used mouse embryonic stem (mES) cells to evaluate the effect of *Pbrm1* gene silencing on sensitivity to a library of 80 small-molecule inhibitors, including those that target oncogenic kinases, DNA repair or cell cycle proteins (Fig. 1A, Table S3). Because loss of ARID2 (another PBAF-specific subunit required for the appropriate incorporation of PBRM1 into the complex) leads to PBRM1 downregulation (1,10,24,25), we carried out a parallel small-molecule inhibitor sensitivity screen using *Arid2* gene silencing (Fig. 1A-C). After siRNA transfection, cells were exposed to increasing concentrations of the 80 small-molecule inhibitors for five days, after which cell viability was assessed using CellTiter-Glo®. Triplicate screens were conducted and Area Under the Curve (AUC) values were calculated for each small-molecule inhibitor transfected either with control, non-targeting siRNA (siCtrl), si*Pbrm1* or si*Arid2*. Using the ratio of AUC values in siCtrl *vs.* si*Pbrm1*-transfected cells, we identified 23 compounds with an AUC ratio > 0.1, including three clinical PARPi (talazoparib, rucaparib and olaparib; ranked #1, #7 and #10, respectively in terms of *Pbrm1* selectivity; Fig. 1D, F, Fig. S1A). *Arid2* silencing also sensitized cells to PARPi (talazoparib, olaparib and rucaparib; ranked #1, #4 and #12 respectively; Fig. 1E, G, Fig. S1B). As loss of ARID2 results in PBRM1 downregulation and misincorporation into PBAF (1,10,24,25), whereas loss of *PBRM1* expression leads to ARID2 upregulation

(10,26) (Fig. S1G, H), we reasoned that both the PBRM1/PARPi and the ARID2/PARPi synthetic lethal effects could operate via impaired PBRM1 function, caused either directly by *PBRM1* mutation, or indirectly, via ARID2 deficiency.

In a second approach, we conducted a parallel small-molecule inhibitor screen in isogenic *PBRM1*-wildtype (WT) and knockout (KO) HAP1 cells (in which *PBRM1* had been inactivated by CRISPR/Cas9 gene editing). Both cell lines were exposed to a library of 167 small-molecule inhibitors (Fig. S1C, Table S4). We identified 37 small-molecule inhibitors with a *PBRM1* AUC ratio > 0.1, including two clinical PARPi (olaparib and veliparib) and two ATR inhibitors (ATRi; VE-822 and VE-821) (Fig. S1D).

In a third screen, we evaluated the synthetic lethality between *PBRM1* gene silencing and silencing of 446 genes implicated in DNA repair and chromatin remodeling (Fig. S1E, Table S5), using a previously described competition-based screening approach in U2OS cells (27). This screen identified synthetic lethal effects between *PBRM1* silencing and siRNAs targeting either *PARP3*, *PARP4*, *PARP1* or *PARP2* (sh*PBRM1* vs shCTRL Z-score difference of -1.47, -0.96, -0.48, and -0.37 respectively, scoring #7, #32, #122 and #152 of all siRNAs; Fig. S1F).

Taken together, these three orthogonal screens, performed in distinct cell line models, suggested that PBRM1 defects caused sensitivity to PARPi, and that these effects were somewhat cell type-independent.

PARP inhibitors elicit *in vitro* synthetic lethality in multiple PBRM1-defective cell line models

In order to validate the synthetic lethal effects of PARPi, we used three chemically-distinct clinical PARPi in five *PBRM1*-isogenic systems and one *PBRM1*-non-isogenic system (Fig. 2, Fig. S2A-H, Fig. S3A-J, Table S1). These included the HAP1 model described earlier where we found that HAP1 *PBRM1*-KO cells were significantly more sensitive to rucaparib, olaparib or talazoparib when compared to *PBRM1*-WT isogenic cells (Fig. 2A; ≈ 10-fold difference in SF_{50}, $p < 0.0001$, two-way ANOVA; Fig. S2A, B). To assess whether these findings could be reproduced in cell lines derived from solid tumors, we created four new *PBRM1*-isogenic models using CRISPR/Cas9 gene editing in 786-O (ccRCC), U2OS (osteosarcoma), H1299 or A549 (NSCLC) cell lines (Fig. S2C, F, Fig. S3A, E). In these models, we found that *PBRM1*-KO cells were more sensitive than *PBRM1*-WT cells to three different clinical PARPi, an effect that was observed using either short-term or long-term PARPi exposure and in both 2D and 3D cultures (Fig. 2B-F, Fig. S2C-H, Fig. S3A-G). To further investigate the generality of this effect, we evaluated PARPi sensitivity in a molecularly diverse, non-isogenic, panel of ccRCC cell lines: PBRM1-proficient 786-O and A498 cells which are homozygous or heterozygous for *VHL* mutations, respectively, and PBRM1-deficient RCC-MF and RCC-FG2 cells, which are *VHL*-wildtype and -mutant, respectively (Fig. S3H). Consistent with the observations made in isogenic systems, loss of PBRM1 expression in ccRCC cell lines was associated with increased sensitivity to PARPi (Fig. 2G, Fig. S3H-J). We noted that the magnitude of the synthetic lethal effects varied from model to model, suggesting that variables other than PBRM1 (such as distinct genetic backgrounds) might also modulate the phenotype.

PARP inhibitor sensitivity is directly linked to PBRM1 deficiency

We next sought to assess whether PARPi sensitivity was directly due to the deficiency in PBRM1. Because defects in ARID1A (a cBAF-specific DNA-binding subunit) and SMARCA4 (a SWI/SNF ATPase and helicase catalytic subunit) have been linked to increased PARPi sensitivity (28–30), we first evaluated ARID1A and SMARCA4 expression in *PBRM1*-isogenic cells. Immunoprecipitation of SMARCC2 (a core subunit of both cBAF and PBAF complexes) followed by western blotting confirmed that ARID1A, SMARCA4, and its paralog SMARCA2, were expressed and incorporated into SWI/SNF complexes even in the absence of PBRM1 (Fig. 2H, Fig. S1G, H and Fig. S4A, B). Consistent with previous work (10,26), we also noted an increase in ARID2 expression in *PBRM1*-KO cells. We also found that in the *SMARCA4*-mutant H1299 and A549 cell lines, the PBAF-specific subunits ARID2 and BRD7 co-immunoprecipitated with SMARCA2, even in the absence of PBRM1 (Fig. S4C-D); reciprocally, SMARCA2 co-immunoprecipitated with ARID2 and BRD7 (Fig. S4E-F). This was consistent with recent reports suggesting that SMARCA2 can compensate for SMARCA4 deficiency, thereby allowing the formation SWI/SNF complexes when SMARCA4 is absent (1,31). To further confirm that PARPi sensitivity was directly linked to PBRM1 deficiency, we re-expressed PBRM1 in 786-O *PBRM1*-KO cells (“PBRM1-rescue model”) using a doxycycline-inducible *PBRM1* cDNA (Fig. 2I). PBRM1 re-expression restored PARPi resistance (Fig. 2J), thereby establishing a causative link between PBRM1 loss-of-function and PARPi sensitivity. Finally, we evaluated the effect of silencing *PBRM1* by shRNA, as partial loss of protein expression might elicit a distinct phenotype to mutation of *PBRM1*. Using multiple shRNA constructs targeting different *PBRM1* sequences (Fig. S4G), we found that sh*PBRM1*-transfected cells were significantly more sensitive to olaparib

than shCTRL-transfected cells (Fig. S4H, I; e.g. at 1 µM olaparib, p = 0.0006 and p = 0.0036 with two different sh*PBRM1*; two-way ANOVA). Together, this data suggested that the enhanced sensitivity to PARPi was directly linked to PBRM1 deficiency.

The PARP inhibitor talazoparib selectively inhibits *PBRM1*-deficient tumor growth in a clear cell renal cell carcinoma xenograft model

To assess the therapeutic potential of PARPi in *PBRM1*-deficient tumors, we evaluated the anti-tumor effect of talazoparib in mice bearing established xenografts derived from either 786-O *PBRM1*-KO or -WT cells (Fig. 2K). Consistent with previous reports (32) and the known tumor suppressive function of PBRM1, we found that *PBRM1*-KO xenografts grew faster *in vivo* than their isogenic *PBRM1*-WT counterparts (Fig. 2L, M). Compared with the drug vehicle, talazoparib treatment impaired the growth of *PBRM1*-KO xenografts, as measured by tumor volume (Fig. 2L, M; p = 0.0001, one-way ANOVA) and tumor weight (Fig. 2N; ≈ 2-fold change, p = 0.0012, one-way ANOVA). Conversely, talazoparib treatment had no effect on *PBRM1*-WT xenografts. Talazoparib also selectively increased the percentage of phosphorylated H2AX (γH2AX)-positive cells in *PBRM1*-KO xenografts collected 28 days after treatment initiation (Fig. S5A, Fig. S5B), suggesting that the latter accumulated more DNA damage when exposed to PARPi.

PBRM1 deficiency is associated with enhanced replication stress and increased genomic instability, which is exacerbated by PARP inhibitors

Sensitivity to PARPi has previously been seen in tumor cells with an ongoing DNA damage response and/or pre-existing DNA damage repair (DDR) defects, notably

those affecting the homologous recombination (HR) pathway (5–7). To investigate whether PBRM1-defective cells exhibited biomarkers of an ongoing DNA damage response, we measured nuclear γH2AX foci in three genetically distinct *PBRM1*-isogenic models. In the absence of exogenous DNA damage, *PBRM1*-KO cells exhibited a higher number of γH2AX foci, compared to *PBRM1*-WT cells (Fig. 3A, B; $p < 0.0001$, Wilcoxon-Mann-Whitney test). Because persisting DNA damage often results in an increased tumor mutational burden (TMB) in cancer (33), we evaluated the TMB of PBRM1-defective tumors. Using whole-exome sequencing (WES) data from the Tumor Cancer Genome Atlas (TCGA), we found that *PBRM1*-mutant tumors from 11 cancer histologies, including ccRCC (KIRC), had a significantly higher TMB than *PBRM1*-wildtype tumors ($p = 0.0009$; Wilcoxon-Mann-Whitney test, Fig. S6A, Tables S6, S7). The analysis of TCGA RNA-Seq data also revealed a negative correlation between *PBRM1* mRNA expression and TMB in several cancer types, including ccRCC (Fig. S6B-E; KIRC, $p < 0.0001$, Wilcoxon-Mann-Whitney test). This suggested that our preclinical observation that PBRM1-deficient cells accumulate DNA damage might also occur in human tumors.

To investigate whether some PBRM1-dependent DDR defects might explain the PBRM1/PARPi synthetic lethality, we exposed three *PBRM1*-isogenic cell lines to PARPi and monitored the presence of γH2AX, RAD51 and RPA foci, which are markers of DNA damage, HR, and single-stranded DNA (ssDNA), respectively. We found a concentration-dependent increase in the number of γH2AX foci after exposure to either olaparib or talazoparib, an effect which was more pronounced in *PBRM1*-KO cells (Fig. 3C, D; Fig. S7A-D; Fig. S8A-D). We also found that the pre-existing number of RAD51 and RPA foci was increased in *PBRM1*-KO cells, and that this phenotype was further exacerbated by PARPi exposure (Fig. 3E, F; Fig. S7E-J;

Fig. S8E-I). We also noted that: (i) mRNA and protein levels of the key HR genes *BRCA1*, *BRCA2* and *RAD51* were similar in *PBRM1*-WT and -KO cells (Fig. S9A, B); (ii) *PBRM1*-KO cells were as sensitive as *PBRM1*-WT cells to ionizing radiation (Fig. S10A-C) and to the DNA DSB-inducing agents etoposide (Fig. S10D-F) and doxorubicin (Fig. S10G-I); and (iii) the number of loss-of-heterozygosity (LOH) events, a correlate genetic marker of HR deficiency, was not increased in *PBRM1*-mutant tumors from the TCGA dataset (Fig. S11) (34). Taken together, these results suggested that *PBRM1*-KO cells are unable to effectively process the DNA damage caused by PARPi, despite no obvious HR defect.

PARP1, when trapped on DNA by PARPi, impairs replication fork (RF) progression and elicits replication stress (35). This triggers the recruitment of ATR via ATRIP, which binds RPA-coated ssDNA at stalled RF. ATR subsequently activates the replication stress response, notably via CHK1 and ATM signaling. Collectively, these events prevent RF collapse and the formation of cytotoxic DSBs. Having previously seen that *PBRM1*-KO cells had pre-existing elevated levels of γH2AX and RPA foci (see above), we assessed replication fork speed in *PBRM1*-isogenic cells by DNA fiber combing (Fig. 3G) and found a significant ≈ 30% decrease in RF velocity in *PBRM1*-KO cells ($p < 0.0001$, Wilcoxon-Mann-Whitney test; Fig. 3H, I). We also found increased expression and phosphorylation of ATR, ATM, and CHK1 in 786-O *PBRM1*-KO cells following cell cycle synchronization using double-thymidine block, a phenotype that was exacerbated by olaparib exposure (Fig. 3J). Similar observations were also made in the HAP1, U2OS and H1299 *PBRM1*-isogenic cells (Fig. S12A-C). Because our initial HAP1 small-molecule inhibitor screen also identified ATRi as being synthetic lethal with PBRM1 defects (Fig. S1D), we recapitulated this observation in *PBRM1*-isogenic cells derived from solid tumors (Fig. S12D-G).

Together, these findings suggested that loss of PBRM1 leads to increased replication stress, which may contribute to PARPi or ATRi sensitivity in *PBRM1*-KO cells (36).

To investigate the consequences of the replication stress observed in PBRM1-deficient cells, we assessed the formation of micronuclei in response to PARPi (37–39) and found that, in the absence of exogenous DNA damage, the proportion of micronuclei-positive cells was significantly higher in *PBRM1*-KO cells (Fig. 3K, L; ≈ 2-fold change, $p < 0.0001$, two-way ANOVA). Exposure to olaparib or talazoparib exacerbated this effect (Fig. 3K, L; Fig. S13A-C), to a degree that was at least equivalent to that caused by the clastogen mitomycin C (used here as a positive control). To investigate the potential sources of micronuclei, we performed time-lapse confocal video-microscopy using an mCherry-labeled histone H2B *PBRM1*-isogenic cells. We found that *PBRM1*-KO cells exhibited a delayed metaphase plate formation, an increased average mitosis duration (45 *vs.* 70 min in *PBRM1*-WT and -KO cells, respectively, $p < 0.0001$, two-way ANOVA; Fig. S14A; Videos S1-4) and a significantly higher number of anaphase bridges and lagging chromosomes compared to *PBRM1*-WT cells (Fig. S14B-D). Together, our data suggested that loss of *PBRM1* leads to increased DNA damage, replication stress and micronuclei formation, effects which were exacerbated by exposure to PARPi.

PBRM1 deficiency associates with increased R-loop formation

R-loops are three-stranded nucleic acid structures that form when an RNA strand invades double-stranded DNA within the chromatin, resulting in an RNA:DNA hybrid and a displaced non-hybridized region of ssDNA. R-loops occur naturally during replication and transcription, but their accumulation is associated with increased

DNA damage, notably under conditions of replication stress (40,41). Having seen that *PBRM1*-KO cells exhibited markers of replication stress, we hypothesized that PBRM1 deficiency may cause this by increasing the burden of R-loops.

To assess this, we used RNA:DNA hybrid dot blot analysis on genomic DNA isolated from 786-O *PBRM1*-isogenic cells using the hybrid-specific S9.6 antibody in the presence or absence of RNase H. This revealed a ≈ 2-fold increase in RNase H-sensitive R-loops in *PBRM1*-KO cells, when compared to *PBRM1*-WT cells (Fig. 4A, B; $p = 0.0113$; Welch's t test). To identify R-loop-enriched sequences in *PBRM1*-KO cells, we used genome-wide DNA:RNA immunoprecipitation sequencing (DRIP-Seq) in duplicate samples of 786-O and H1299 *PBRM1*-isogenic cells, cultured in the presence or absence of PARPi (Fig. S15A). Principal Component Analysis (PCA) confirmed high reproducibility between duplicates (Fig. 4C, Fig. S15B). Input and RNase H-treated conditions were used to evaluate the specificity of S9.6-associated peaks. We found that *PBRM1*-KO cells displayed a ≈ 2-fold higher number of RNase H-sensitive DRIP-Seq peaks compared to their *PBRM1*-WT counterparts (Fig. 4D-F, Fig. S15C). When analyzing the genomic localization of DRIP-Seq peaks, we found that 90% of the peaks identified in *PBRM1*-WT cells were also present at the same genomic locus in *PBRM1*-KO isogenic cells. Strikingly, *PBRM1*-KO cells exhibited numerous additional peaks that were not detected in *PBRM1*-WT cells (Fig. 4E, F), notably in introns or intron-promoter spanning regions (Fig. 4G, Fig. S15D, Fig. S16A, B), suggesting an increased formation or defective resolution of R-loops when PBRM1 was absent. Exposure to PARPi did not modify the total number of genomic loci with DRIP-Seq peaks in *PBRM1*-WT or -KO models (Fig. S16C-F) but did increase the total R-loop burden in *PBRM1*-KO cell lines at consensus peaks (defined as peaks present in at least two independent samples from a given isogenic

model; Fig. 4H, Fig. S17A). Taken together, this data suggested that PARPi exposure might stabilize or prevent the resolution of pre-existing R-loops in *PBRM1*-KO cells, rather than leading to the formation of new R-loops.

To investigate the potential role of R-loop in PARPi sensitivity, we overexpressed RNase H1, an endonuclease responsible for R-loop degradation, in *PBRM1*-isogenic cells (Fig. 4I). Overexpression of RNase H1 in H1299 *PBRM1*-KO cells partially restored talazoparib resistance, an effect that was less pronounced in *PBRM1*-WT cells (Fig. 4J). As R-loops are transcriptional by-products (41), we also assessed whether silencing transcription in *PBRM1*-KO cells could restore resistance to PARPi. We exposed *PBRM1*-isogenic cells to olaparib in the presence or absence of 5,6-dichlorobenzimidazole 1-β-D-ribofuranoside (DRB, an inhibitor of RNA polymerase II-mediated transcription elongation) and found that DRB reduced the sensitivity of *PBRM1*-KO cells – but not *PBRM1*-WT cells – to PARPi (Fig. 4K), while both *PBRM1*-WT and -KO cells displayed similar sensitivity to DRB when used as a monotherapy (Fig. S17B).

To explore the cause of R-loop accumulation in *PBRM1*-KO cells, we generated mass spectrometry proteomic profiles of HAP1 *PBRM1*-isogenic cells. We found a significant downregulation of more than 20 proteins involved in R-loop resolution, including RNase H1, SETX, DHX9, XRN2 and BLM (Log_2(FC) = -0.460, FDR = 0.0083; Log_2(FC) = -0.366, FDR = 0.0006; Log_2(FC) = -0.197, FDR = 0.0019; Log_2(FC) = -0.193, FDR = 0.0024; Log_2(FC) = -0.476, FDR = 0.0002, respectively; Fig. S17C). Using TCGA data, we further explored whether such a correlation also existed in human tumors. Consistent with our findings in HAP1 cells, we found that mRNA expression of several R-loop processing factors, including *SETX*, *DHX9* and

XRN2, correlated with *PBRM1* mRNA expression in the TCGA ccRCC and NSCLC cohorts (Spearman's correlation coefficient r = 0.72, 0.47, 0.40, all p < 0.0001, for *SETX*, *DHX9* and *XRN2* in KIRC, respectively; Fig. S17D-F). Using the 786-O "PBRM1-rescue" isogenic model, we also found that 786-O *PBRM1*-KO cells exhibited decreased SETX expression, which was reversed by *PBRM1* re-expression (Fig. S17G).

To assess the potential significance of SETX downregulation in PBRM1-deficient cells, we used a CRISPR/Cas9-mediated activation (CRIPSRa) approach to drive *SETX* expression in *PBRM1*-isogenic cells (Fig. S18A, B), and evaluated the effect of this genetic perturbation on PARPi sensitivity. Using two different single-guide RNAs targeting the *SETX* promoter region, we found that *SETX* overexpression led to increased resistance of H1299 *PBRM1*-KO (but not *PBRM1*-WT) cells to both olaparib and talazoparib (Fig. S18C-E). These observations suggested that loss of PBRM1 is associated with a downregulation of several factors involved in R-loop processing, which might play a role in the accumulation of these structures in *PBRM1*-KO cells.

PARP and ATR inhibitors induce a cell-autonomous cGAS/STING response in PBRM1-defective cells

The cytosolic DNA sensing cyclic GMP-AMP synthase / stimulator of interferon genes (cGAS/STING) pathway detects cytosolic DNA (often the by-product of viral infection, DNA damage or replication stress) and in turn activates type I interferon innate immune signaling (42). PARPi-induced activation of cGAS/STING following micronuclei formation and the generation of cytosolic DNA, is now recognized as an important component of PARPi-mediated synthetic lethal effects (23,43–45). Recent

reports also suggest that R-loops may contribute to cGAS/STING activation (40,46). Moreover, the cGAS/STING pathway plays an essential role in the therapeutic effect of immune checkpoint inhibitors (ICI) (47,48), a standard-of-care in ccRCC and NSCLC, two histologies where *PBRM1* is frequently mutated. Given this, we assessed whether PARPi or ATRi activated cGAS/STING signaling in PBRM1-defective ccRCC and NSCLC cells, as PARPi are known to do in *BRCA*-mutant tumor cells (23,45,49). To assess this, we measured three sequentially-occurring phenotypes that are linked to PARPi-mediated cGAS/STING pathway activation and anti-tumor immunity: (i) the accumulation of cytosolic DNA in the form of micronuclei; (ii) the phosphorylation of TANK-binding kinase 1 (TBK1) and interferon regulatory factor 3 (IRF3); (iii) the induction of a type I interferon response (23,43,44).

Consistent with our previous observations (Fig. 3K, L), pre-existing levels of micronuclei were higher in *PBRM1*-KO cells compared to *PBRM1*-WT cells (Fig. 5A; Fig. S19A, B). Exposure to PARPi or ATRi resulted in a concentration-dependent accumulation of micronuclei in both H1299 and 786-O *PBRM1*-isogenic cells, an effect that was more pronounced in *PBRM1*-KO cells (Fig. 5A-C). Western blot analyses also revealed a concentration- and PBRM1-dependent increase in TBK1 and IRF3 phosphorylation levels in H1299 isogenic cells exposed to PARPi or ATRi (Fig. 5D, Fig. S19C, D). Using RT-qPCR, we also found that VE-822 exposure caused a significantly more profound induction of *CCL5* and *CXCL10* mRNA in H1299 *PBRM1*-KO cells compared to -WT cells, by more than 2-fold and 4-fold, respectively ($p < 0.0001$; Welch's t-test; Fig. 5E, F). Intriguingly, such selectivity was not observed in the 786-O *PBRM1*-isogenic model, in which *CCL5* mRNA expression was only significantly induced in the *PBRM1*-WT cell line at the VE-822 concentration that caused a significant increase in micronuclei number (Fig. 5C, Fig.

S19E, F). This prompted us to explore the expression of cGAS and STING in these models, as loss of cGAS or STING has recently been described as an important and independent determinant of cancer cell immunogenicity in other DDR-defective contexts (48). We found that cGAS protein expression was decreased in 786-O *PBRM1*-KO cells compared to -WT cells (Fig. S19G, Fig. S20), suggesting that defective cGAS/STING signaling might underly the absence of cell-autonomous immunity activation in the 786-O *PBRM1*-KO cell line, despite a significant micronuclei accumulation upon PARPi and ATRi exposure. To further investigate whether expression of cGAS and STING was necessary for ATRi-induced type I interferon response, we silenced *CGAS* and *STING*-coding genes by siRNA, and measured *CCL5* and *CXCL10* mRNA expression levels upon ATRi exposure. Silencing of *CGAS* and *STING* abrogated *CCL5* and *CXCL10* mRNA induction in both H1299 and 786-O *PBRM1*-isogenic models, thereby supporting a direct role for the cGAS/STING pathway in mediating ATRi-induced type I interferon response (Fig. 5E, F; Fig. S19E, F). Altogether, these findings suggested that cytosolic DNA sensing in tumor cells via cGAS/STING could be an essential determinant of the cell-autonomous immunomodulatory potential of PARPi and ATRi in PBRM1-deficient ccRCC and NSCLC cells.

Discussion

PBRM1 defects are frequent in human cancers. There is currently no approved precision medicine-based approach to specifically target deficiency in this PBAF-specific subunit. Here, we show that clinical PARPi and ATRi are synthetic lethal with *PBRM1* defects. These genetic vulnerabilities, which we reproduced in multiple isogenic and non-isogenic models from various genetic backgrounds, appear to be

cell type-independent, suggesting that these findings might have translational utility in several cancer types where *PBRM1* is mutated.

The three distinct forms of mSWI/SNF complexes (cBAF, PBAF, and non-canonical BAF), assemble following an ordered, modular pathway, and have different functions and composition (31). PBRM1 is a specific subunit of the PBAF complex and, interestingly, it is the last subunit to be incorporated into PBAF (1). Notably, PBRM1 deletion has no effect on PBAF assembly (1), which supports that the PBRM1/PARPi SL is directly linked to PBRM1 loss, and is in line with our findings (Fig. 2H-J). This also suggests that the PBRM1/PARPi SL is distinct from other synthetic lethalities that have been recently described between PARPi or ATRi, and the cBAF-specific ARID1A subunit or the ATPase SMARCA4 subunit (29,50–52). Therefore, to our knowledge, our manuscript describes, for the first time, that defects in a PBAF-specific subunit (PBRM1) associate with R-loop accumulation, and lead to increased sensitivity to PARPi and ATRi. This has important clinical implications, given that PBRM1 defects occur in a clinically-distinct patient population than ARID1A or SMARCA4 defects, where the use of PARPi or ATRi has not previously been proposed.

In Fig. 6, we propose a working model to explain our findings. Exposure to PARPi or ATRi causes increased replication stress. In the case of PARPi, this is likely due to the accumulation of trapped-PARP1 lesions, while in the case of ATRi, this might be because of the relative inability of tumor cells to effectively respond to replication stress caused by endogenous factors. When *PBRM1* function is intact (Fig. 6A), the induced replication stress remains limited, possibly due to PBRM1-mediated replication fork re-priming (6) and ATM-dependent transcriptional silencing around

DSBs (7). This limited replication stress associates with residual levels of DNA damage and a moderate formation of micronuclei, which, in itself, is insufficient to activate the cGAS/STING signaling response. In PBRM1-deficient tumor cells (Fig. 6B), impaired DDR (Fig. 3) (6–8) and higher R-loop burden (Fig. 4) likely contribute to enhance replication stress and DNA damage (41). Exposure to PARPi or ATRi in the presence of a PBRM1 defect (Fig. 6C) further exacerbates replication stress, promoting DNA damage accumulation and micronuclei formation. This triggers a cell-autonomous type I interferon response, in a cGAS/STING-dependent manner (Fig. 5). Upon prolonged exposure to PARPi or ATRi, the extent of DNA damage eventually reaches levels that are no longer compatible with cell survival (Fig. 2).

Alternative or additional mechanisms might also contribute to the PBRM1/DNA repair inhibitor synthetic lethality. R-loops induce a DDR that can be mediated by ATM and/or ATR (40). Because PBRM1 participates in ATM-dependent transcriptional repression at DSBs (7), it is possible that in the absence of PBRM1, the resulting transcriptional silencing defects favor the accumulation of R-loops. The partial reversal of PARPi sensitivity observed when transcription is pharmacologically silenced may support this first alternative model. It is also possible that PBRM1-defective cells present increased transcriptional stress, which is further exacerbated by PARPi. Indeed, R-loop-dependent transcriptional stress can cause DNA damage by sequestering BRCA1 at sites of stalled RNA polymerase II (53), where BRCA1 recruits SETX to prevent DNA damage (54,55). As SETX is also recruited at sites of DNA DSBs in transcriptionally active loci (56), a transcriptional stress-dependent sensitivity to DNA repair inhibitors represents a second alternative model. This secondary model is consistent with the previously described role of PBRM1 in regulating the transcription of stress response genes and in mediating the

cytoprotective effects against endogenous oncogenic, replicative stresses (57,58), or exogenous stresses (59). A third alternative model to explain the PBRM1/DNA repair inhibitors synthetic lethality may be that PBRM1, which contributes to replication fork re-priming through PCNA recruitment (6), might also interact with other chromatin remodelers that are ATR substrates and promote replication fork repair, such as the SWI/SNF-family member SMARCAL1 (60).

We and others previously described that PARPi have cell-autonomous immunomodulatory properties, which activate the cGAS/STING signaling cascade in DDR-defective genetic contexts (23,43,44,61). However, very little is known about the immunomodulatory properties of ATRi. Here, we describe that ATRi can trigger a cell-autonomous type I interferon response through cGAS/STING activation. In line with our results, it was recently suggested that ATRi enhance interferon responses in combination with radiotherapy (62). Because several clinical ATRi are currently being developed, notably in combination with ICI (NCT02264678), assessing whether ATRi-dependent immunomodulation also occurs in genetic contexts where ATRi elicit synthetic lethality (50,51) could have direct clinical implications.

Interestingly, *PBRM1* loss-of-function has recently been associated with enhanced tumor cell sensitivity to interferon-γ and increased type I interferon response (10). PBRM1 defects were further linked to better survival upon anti-PD-1 and anti-CTLA-4 therapy in mice (10), as well as enhanced efficacy of anti-PD-(L)1 therapy in patients with ccRCC (9,63). Controversially, other studies reported that *Pbrm1* inactivation resulted in a non-immunogenic tumor microenvironment favoring resistance to anti-PD-1 therapy in murine ccRCC models (64), and that *PBRM1* mutation did not correlate with clinical benefit in patients treated with ICI (18,64,65).

Investigating whether the inconstant sensitivity of PBRM1-deficient tumors to ICI results from variable cytosolic DNA sensing capacities within tumor cells, notably that of the cGAS/STING pathway as recently described in mismatch repair deficient contexts (48), is an important question that warrants further exploration.

In conclusion, our findings shed light on the genetic vulnerabilities associated with loss of PBRM1 related to its role in maintaining genome integrity. We are currently exploring the PARPi plus anti-PD-L1 combination therapy in patients with ccRCC, in an investigator-initiated academic phase II study developed on the basis of our preclinical findings (EudraCT N° 2018-001744-62).

Authors' Contribution

Conception and design: RMC, DM, CJL, SPV.

Development of methodology: RMC, DM, LCD, TE, ND, MG, AL, CJL, SPV.

Acquisition of data (provided animals, provided facilities, etc.): RMC, DM, LCD, TE, IB, ND, MG, SH, CM, AL, TIR, SJ, AK.

Analysis and interpretation of data: RMC, DM, LCD, TE, IB, ND, MG, CN, AL, SJ, AK, CJL, SPV.

Writing, review, and/or revision of the manuscript: All authors.

Administrative, technical, or material support: RMC, DM, LCD, TE, IB, ND, MG, AL, SJ, AK, JSC, JCS, JD, CJL, SPV.

Study supervision: CJL, SPV.

Acknowledgements

This work was funded by programme grants to SPV from Institut National de la Santé et de la Recherche Médicale (INSERM ATIP-Avenir Programme Funding), Site de Recherche Intégrée sur le Cancer SOCRATE-2 (INCa-DGOS-INSERM_12551), Cancéropôle Ile-de-France (2017-1-EMERG-72), and Association pour la Recherche contre le Cancer (PGA1 RF 20190208576), as well as programme grants to CJL from Cancer Research UK (CRUK Programme Funding C30061/A24439) and Breast Cancer Now as part of programme funding to the Breast Cancer Now Toby Robins Research Centre. RMC received award funding from Fondation Bettencourt-Schueller, Institut Servier, Fondation des Treilles and Cancéropôle Ile-De-France. DM received funding from the INSERM ITMO Cancer grant. This study represents independent research supported by the National Institute for Health Research (NIHR) Biomedical Research Centre at The Royal Marsden NHS Foundation Trust and The Institute of Cancer Research, London. The views expressed are those of the author(s) and not necessarily those of the NIHR or the Department of Health and Social Care.

We would like to thank Dr. Marjorie Drac and Dr. Etienne Schwob, as well as the Genomic Vision team for performing some DNA combing experiments related to this project. We thank Dr. Damien Drubay for his help with the statistical analyses.

References

1. Mashtalir N, D'Avino AR, Michel BC, Luo J, Pan J, Otto JE, et al. Modular Organization and Assembly of SWI/SNF Family Chromatin Remodeling Complexes. Cell. 2018;175:1272–88.
2. Charlop-Powers Z, Zeng L, Zhang Q, Zhou MM. Structural insights into selective histone H3 recognition by the human Polybromo bromodomain 2. Cell Research. 2010;20:529–38.
3. Duan MR, Smerdon MJ. Histone H3 lysine 14 (H3K14) acetylation facilitates DNA repair in a positioned nucleosome by stabilizing the binding of the chromatin remodeler RSC (Remodels Structure of Chromatin). Journal of Biological Chemistry. 2014;289:8353–63.
4. Slaughter MJ, Shanle EK, McFadden AW, Hollis ES, Suttle LE, Strahl BD, et al. PBRM1 bromodomains variably influence nucleosome interactions and cellular function. Journal of Biological Chemistry. 2018;293:13592–603.
5. Brownlee PM, Chambers AL, Cloney R, Bianchi A, Downs JA. BAF180 Promotes Cohesion and Prevents Genome Instability and Aneuploidy. Cell Reports. 2014;6:973–81.
6. Niimi A, Chambers AL, Downs JA, Lehmann AR. A role for chromatin remodellers in replication of damaged DNA. Nucleic Acids Research. 2012;40:7393–403.
7. Kakarougkas A, Ismail A, Chambers AL, Riballo E, Herbert AD, Künzel J, et al. Requirement for PBAF in Transcriptional Repression and Repair at DNA Breaks in Actively Transcribed Regions of Chromatin. Molecular Cell. 2014;55:723–32.
8. Meisenberg C, Pinder SI, Hopkins SR, Wooller SK, Benstead-Hume G, Pearl FMG, et al. Repression of Transcription at DNA Breaks Requires Cohesin throughout Interphase and Prevents Genome Instability. Molecular Cell. 2019;73:212–23.
9. Miao D, Margolis CA, Gao W, Voss MH, Li W, Martini DJ, et al. Genomic correlates of response to immune checkpoint therapies in clear cell renal cell carcinoma. Science. 2018;359:801–6.

10. Pan D, Kobayashi A, Jiang P, de Andrade LF, Tay RE, Luoma AM, et al. A major chromatin regulator determines resistance of tumor cells to T cell-mediated killing. Science. 2018;359:770–5.
11. Gerlinger M, Horswell S, Larkin J, Rowan AJ, Salm MP, Varela I, et al. Genomic architecture and evolution of clear cell renal cell carcinomas defined by multiregion sequencing. Nature Genetics. 2014;46:225–33.
12. Pawłowski R, Mühl SM, Sulser T, Krek W, Moch H, Schraml P. Loss of PBRM1 expression is associated with renal cell carcinoma progression. International Journal of Cancer. 2013;132:E11-7.
13. Eckel-Passow JE, Serie DJ, Cheville JC, Ho TH, Kapur P, Brugarolas J, et al. BAP1 and PBRM1 in metastatic clear cell renal cell carcinoma: tumor heterogeneity and concordance with paired primary tumor. BMC Urology. 2017;17:19.
14. Bihr S, Ohashi R, Moore AL, Rüschoff JH, Beisel C, Hermanns T, et al. Expression and Mutation Patterns of PBRM1, BAP1 and SETD2 Mirror Specific Evolutionary Subtypes in Clear Cell Renal Cell Carcinoma. Neoplasia (United States). 2019;21:247–56.
15. de Velasco G, Wankowicz SA, Madison R, Ali SM, Norton C, Duquette A, et al. Targeted genomic landscape of metastases compared to primary tumours in clear cell metastatic renal cell carcinoma. British Journal of Cancer. 2018;118:1238–42.
16. Bratslavsky G, Gay LM, Sokol E, Elvin JA, Vergilio J-A, Suh J, et al. PBRM1 mutation and immunotherapy efficacy: A comprehensive genomic profiling (CGP) assessment. Journal of Clinical Oncology. 2018;36.
17. Wang L, Zehir A, Nafa K, Zhou N, Berger MF, Casanova J, et al. Genomic aberrations frequently alter chromatin regulatory genes in chordoma. Genes Chromosomes and Cancer. 2016;55:591–600.
18. Zhou H, Liu J, Zhang Y, Huang Y, Shen J, Yang Y, et al. PBRM1 mutation and preliminary response to immune checkpoint blockade treatment in NSCLC. npj Precision Oncology. 2020;4.
19. Chabanon RM, Morel D, Postel-Vinay S. Exploiting epigenetic vulnerabilities in solid tumors: Novel therapeutic opportunities in the treatment of SWI/SNF-defective cancers. Seminars in Cancer Biology. 2020;61:180–98.

20. Morel D, Almouzni G, Soria JC, Postel-Vinay S. Targeting chromatin defects in selected solid tumors based on oncogene addiction, synthetic lethality and epigenetic antagonism. Annals of Oncology. 2017;28:254–69.
21. Bajrami I, Marlow R, van de Ven M, Brough R, Pemberton HN, Frankum J, et al. E-Cadherin/ROS1 inhibitor synthetic lethality in breast cancer. Cancer Discovery. 2018;8:498–515.
22. Bialic M, Coulon V, Drac M, Gostan T, Schwob E. Analyzing the dynamics of DNA replication in mammalian cells using DNA combing. Methods in Molecular Biology. 2015;1300:67–78.
23. Chabanon RM, Muirhead G, Krastev DB, Adam J, Morel D, Garrido M, et al. PARP inhibition enhances tumor cell–intrinsic immunity in ERCC1-deficient non–small cell lung cancer. Journal of Clinical Investigation. 2019;129:1211–28.
24. Roumeliotis TI, Williams SP, Gonçalves E, Alsinet C, del Castillo Velasco-Herrera M, Aben N, et al. Genomic Determinants of Protein Abundance Variation in Colorectal Cancer Cells. Cell Reports. 2017;20:2201–14.
25. Yan Z, Cui K, Murray DM, Ling C, Xue Y, Gerstein A, et al. PBAF chromatin-remodeling complex requires a novel specificity subunit, BAF200, to regulate expression of selective interferon-responsive genes. Genes and Development. 2005;19:1662–7.
26. Chowdhury B, Porter EG, Stewart JC, Ferreira CR, Schipma MJ, Dykhuizen EC. PBRM1 regulates the expression of genes involved in metabolism and cell adhesion in renal clear cell carcinoma. PLoS ONE. 2016;11:e0153718.
27. Hopkins SR, McGregor GA, Murray JM, Downs JA, Savic V. Novel synthetic lethality screening method identifies TIP60-dependent radiation sensitivity in the absence of BAF180. DNA Repair. 2016;46:47–54.
28. Park Y, Chui MH, Rahmanto YS, Yu ZC, Shamanna RA, Bellani MA, et al. Loss of ARID1A in tumor cells renders selective vulnerability to combined ionizing radiation and PARP inhibitor therapy. Clinical Cancer Research. 2019;25:5584–94.
29. Shen J, Peng Y, Wei L, Zhang W, Yang L, Lan L, et al. ARID1A Deficiency Impairs the DNA Damage Checkpoint and Sensitizes Cells to PARP Inhibitors. Cancer discovery. 2015;5:752–67.

30. Smith-Roe SL, Nakamura J, Holley D, Chastain PD, Rosson GB, Simpson DA, et al. SWI/SNF complexes are required for full activation of the DNA-damage response. Oncotarget. 2015;6:732–45.
31. Michel BC, D'Avino AR, Cassel SH, Mashtalir N, McKenzie ZM, McBride MJ, et al. A non-canonical SWI/SNF complex is a synthetic lethal target in cancers driven by BAF complex perturbation. Nature Cell Biology. 2018;20:1410–20.
32. Cai W, Su L, Liao L, Liu ZZ, Langbein L, Dulaimi E, et al. PBRM1 acts as a p53 lysine-acetylation reader to suppress renal tumor growth. Nature Communications. 2019;10:5800.
33. Chabanon RM, Pedrero M, Lefebvre C, Marabelle A, Soria JC, Postel-Vinay S. Mutational landscape and sensitivity to immune checkpoint blockers. Clinical Cancer Research. 2016;22:4309–21.
34. Thorsson V, Gibbs DL, Brown SD, Wolf D, Bortone DS, Ou Yang TH, et al. The Immune Landscape of Cancer. Immunity. 2018;51:411–2.
35. Lord CJ, Ashworth A. PARP inhibitors: Synthetic lethality in the clinic. Science. 2017;355:1152–8.
36. Slade D. PARP and PARG inhibitors in cancer treatment. Genes and Development. 2020;34:360–94.
37. Wilhelm T, Olziersky AM, Harry D, de Sousa F, Vassal H, Eskat A, et al. Mild replication stress causes chromosome mis-segregation via premature centriole disengagement. Nature Communications. 2019;10:3585.
38. Harding SM, Benci JL, Irianto J, Discher DE, Minn AJ, Greenberg RA. Mitotic progression following DNA damage enables pattern recognition within micronuclei. Nature. 2017;548:466–70.
39. Ubhi T, Brown GW. Exploiting DNA replication stress for cancer treatment. Cancer Research. 2019;79:1730–9.
40. Crossley MP, Bocek M, Cimprich KA. R-Loops as Cellular Regulators and Genomic Threats. Molecular Cell. 2019;73:398–411.
41. Aguilera A, García-Muse T. R Loops: From Transcription Byproducts to Threats to Genome Stability. Molecular Cell. 2012;46:115–24.
42. Hopfner KP, Hornung V. Molecular mechanisms and cellular functions of cGAS–STING signalling. Nature Reviews Molecular Cell Biology. 2020;21:501–21.

43. Pantelidou C, Sonzogni O, Taveira MDO, Mehta AK, Kothari A, Wang D, et al. PARP inhibitor efficacy depends on CD8+ T-cell recruitment via intratumoral STING pathway activation in BRCA-deficient models of triple-negative breast cancer. Cancer Discovery. 2019;9:722–37.

44. Ding L, Kim HJ, Wang Q, Kearns M, Jiang T, Ohlson CE, et al. PARP Inhibition Elicits STING-Dependent Antitumor Immunity in Brca1-Deficient Ovarian Cancer. Cell Reports. 2018;25:2972–80.

45. Chopra N, Tovey H, Pearson A, Cutts R, Toms C, Proszek P, et al. Homologous recombination DNA repair deficiency and PARP inhibition activity in primary triple negative breast cancer. Nature Communications. 2020;11:2662.

46. Mankan AK, Schmidt T, Chauhan D, Goldeck M, Höning K, Gaidt M, et al. Cytosolic RNA:DNA hybrids activate the cGAS –STING axis. The EMBO Journal. 2014;33:2937–46.

47. Wang H, Hu S, Chen X, Shi H, Chen C, Sun L, et al. cGAS is essential for the antitumor effect of immune checkpoint blockade. Proceedings of the National Academy of Sciences of the United States of America. 2017;114:1637–42.

48. Lu C, Guan J, Lu S, Diaz LA, Lu C, Guan J, et al. DNA Sensing in Mismatch Repair-Deficient Tumor Cells Is Essential for Anti-tumor Immunity. Cancer Cell. 2020;S1535-6108:30598–5.

49. Parkes EE, Walker SM, Taggart LE, McCabe N, Knight LA, Wilkinson R, et al. Activation of STING-Dependent Innate Immune Signaling By S-Phase-Specific DNA Damage in Breast Cancer. Journal of the National Cancer Institute. 2017;109:djw199.

50. Williamson CT, Miller R, Pemberton HN, Jones SE, Campbell J, Konde A, et al. ATR inhibitors as a synthetic lethal therapy for tumours deficient in ARID1A. Nature Communications. 2016;7:13837.

51. Kurashima K, Kashiwagi H, Shimomura I, Suzuki A, Takeshita F, Mazevet M, et al. SMARCA4 deficiency-associated heterochromatin induces intrinsic DNA replication stress and susceptibility to ATR inhibition in lung adenocarcinoma. NAR Cancer. 2020;2:zcaa005.

52. Gupta M, Concepcion CP, Fahey CG, Keshishian H, Bhutkar A, Brainson CF, et al. BRG1 Loss Predisposes Lung Cancers to Replicative Stress and ATR Dependency. Cancer Research. 2020;80:3841–54.
53. Gorthi A, Romero JC, Loranc E, Cao L, Lawrence LA, Goodale E, et al. EWS-FLI1 increases transcription to cause R-Loops and block BRCA1 repair in Ewing sarcoma. Nature. 2018;555:387–91.
54. Shivji MKK, Renaudin X, Williams ÇH, Venkitaraman AR. BRCA2 Regulates Transcription Elongation by RNA Polymerase II to Prevent R-Loop Accumulation. Cell Reports. 2018;22:1031–9.
55. Hatchi E, Skourti-Stathaki K, Ventz S, Pinello L, Yen A, Kamieniarz-Gdula K, et al. BRCA1 recruitment to transcriptional pause sites is required for R-loop-driven DNA damage repair. Molecular Cell. 2015;57:636–47.
56. Cohen S, Puget N, Lin YL, Clouaire T, Aguirrebengoa M, Rocher V, et al. Senataxin resolves RNA:DNA hybrids forming at DNA double-strand breaks to prevent translocations. Nature Communications. 2018;9:533.
57. Burrows AE, Smogorzewska A, Elledge SJ. Polybromo-associated BRG1-associated factor components BRD7 and BAF180 are critical regulators of p53 required for induction of replicative senescence. Proceedings of the National Academy of Sciences of the United States of America. 2010;107:14280–5.
58. Espana-Agusti J, Warren A, Chew SK, Adams DJ, Matakidou A. Loss of PBRM1 rescues VHL dependent replication stress to promote renal carcinogenesis. Nature Communications. 2017;8:2026.
59. Porter EG, Dhiman A, Chowdhury B, Carter BC, Lin H, Stewart JC, et al. PBRM1 Regulates Stress Response in Epithelial Cells. iScience. 2019;15:196–210.
60. Couch FB, Bansbach CE, Driscoll R, Luzwick JW, Glick GG, Bétous R, et al. ATR phosphorylates SMARCAL1 to prevent replication fork collapse. Genes and Development. 2013;27:1610–23.
61. Sen T, Rodriguez BL, Chen L, della Corte CM, Morikawa N, Fujimoto J, et al. Targeting DNA damage response promotes antitumor immunity through STING-mediated T-cell activation in small cell lung cancer. Cancer Discovery. 2019;9:646–61.

62. Dillon MT, Bergerhoff KF, Pedersen M, Whittock H, Crespo-Rodriguez E, Patin EC, et al. ATR inhibition potentiates the radiation-induced inflammatory tumor microenvironment. Clinical Cancer Research. 2019;25:3392–403.

63. Braun DA, Ishii Y, Walsh AM, van Allen EM, Wu CJ, Shukla SA, et al. Clinical Validation of PBRM1 Alterations as a Marker of Immune Checkpoint Inhibitor Response in Renal Cell Carcinoma. JAMA Oncology. 2019;5:1631–3.

64. Liu X de, Kong W, Peterson CB, McGrail DJ, Hoang A, Zhang X, et al. PBRM1 loss defines a nonimmunogenic tumor phenotype associated with checkpoint inhibitor resistance in renal carcinoma. Nature Communications. 2020;11:2135.

65. McDermott DF, Huseni MA, Atkins MB, Motzer RJ, Rini BI, Escudier B, et al. Clinical activity and molecular correlates of response to atezolizumab alone or in combination with bevacizumab versus sunitinib in renal cell carcinoma. Nature Medicine. 2018;24:749–57.

Figure Legends

Figure 1. A small-molecule inhibitor screen identifies that PBRM1 is synthetic lethal with PARP inhibition. A, Schematic representation describing the workflow of the siRNA small-molecule inhibitor-sensitization screen performed in mouse Embryonic Stem (mES) cells. **B, C,** Western blot of PBRM1 (**B**) and ARID2 (**C**) expression in mES cells transfected with siRNAs targeting *Pbrm1*, *Arid2* or a control, non-targeting, siRNA (siCtrl). Whole cell lysates were extracted 72 hours post-transfection, and probed with the corresponding antibodies. **D, E,** Bar plots displaying the 80 tested small-molecules ranked by decreasing normalized AUC difference between siCtrl and si*Pbrm1* (**D**) or si*Arid2* (**E**); PARP inhibitors are highlighted in red; the normalized AUC differences were calculated as (AUC_{siCtrl} - $AUC_{si\textit{Pbrm1}}$) / AUC_{siCtrl} and (AUC_{siCtrl} - $AUC_{si\textit{Arid2}}$) / AUC_{siCtrl}. **F, G,** Surviving fractions of the small-molecule inhibitor screen upon exposure to clinical PARP inhibitors after *Pbrm1* (**F**) or *Arid2* (**G**) silencing in mES cells. Mean ± SD; two-way ANOVA.

Figure 2. PBRM1 deficiency causes sensitivity to PARP inhibitors. A, B, C, Dose-response survival curves of *PBRM1*-isogenic HAP1 (**A**), H1299 (**B**), and U2OS (**C**) cells exposed to increasing concentrations of the clinical PARPi rucaparib or talazoparib for 7-days in short-term survival assay. Mean ± SD, *n* = 3; two-way ANOVA. **D, E, F,** Dose-response survival curves of *PBRM1*-isogenic H1299 (**D**), 786-O (**E**) and U2OS (**F**) cells exposed to increasing concentrations of the clinical PARPi talazoparib for 14 days in colony-formation assay. Mean ± SD, *n* = 3; two-way ANOVA. To the right of each panel are representative images of corresponding colony-formation assays. **G,** Dose-response survival curves of *PBRM1*-proficient (786-O, A498) or *PBRM1*-deficient (RCC-MF, RCC-FG2) ccRCC lines exposed to increasing concentrations of talazoparib for 14 days in colony-formation assay. Mean ± SD, *n* = 3; two-way ANOVA. **H**, Western blot of selected SWI/SNF subunit expression on total cell extracts following immunoprecipitation of SMARCC2 in U2OS *PBRM1*-isogenic (left) and 786-O *PBRM1*-isogenic (right) cells. Input, immunoprecipitated

(IP) and flow-through (FT) fractions are shown. **I,** Western blot of PBRM1 expression in total cell extracts of 786-O *PBRM1*-isogenic cells before and after transduction with a doxycycline-inducible construct containing *PBRM1* cDNA in the absence (+ *PBRM1* cDNA) or presence (+ *PBRM1* cDNA + Dox) of doxycycline. **J,** Spheroid growth of 786-O *PBRM1*-isogenic cells (as described in **I**) after 16 days of treatment with talazoparib at the *PBRM1*-KO model SF_{20} (5 µM). Mean ± SD, *n* = 3; two-way ANOVA and *post hoc* Tukey's test, relative to DMSO control. **K,** Schematic representation of the therapeutic experiment evaluating talazoparib anti-tumor efficacy in mice with established 786-O *PBRM1*-isogenic xenografts. NSG mice were implanted with 786-O *PBRM1*-isogenic tumor chunks. Once the tumor reached 40 mm^3 volume, mice were randomized to receive vehicle (N = 11 for *PBRM1*-WT; N = 10 for *PBRM1*-KO) or talazoparib (0.2mg/kg daily by oral gavage; N = 11 for *PBRM1*-WT; N = 9 for *PBRM1*-KO). Tumor volume was monitored twice weekly during 28 days. **L, M,** Therapeutic responses to talazoparib treatment in mice bearing *PBRM1*-WT (**L**) or *PBRM1*-KO (**M**) tumors. Mean tumor volume ± SD; two-way ANOVA and *post hoc* Dunnett's test. **N,** Tumor weight (in g) at time of mice sacrifice. Mean ± SD; one-way ANOVA and post hoc Sidak's test.

Figure 3. PBRM1-deficient cells exhibit replication stress and selectively accumulate DNA damage in response to PARP inhibitors. A, **B**, Quantification of the baseline number of γH2AX foci per nuclei in 786-O (**A**) and U2OS (**B**) *PBRM1*-isogenic cells. A minimum of 250 nuclei per condition were analyzed. Mean ± SD; Wilcoxon-Mann-Whitney test. Data from one representative biological replicate of three independent experiments are shown. **C**, Representative immunofluorescence images of γH2AX and RAD51 foci in DMSO- and olaparib-treated 786-O *PBRM1*-isogenic cells. Cells were exposed to 5 µM olaparib or DMSO (vehicle) for 48 hr. Scale bar: 20 µm. **D**, **E**, **F**, Automated quantification of γH2AX (**D**), RAD51 (**E**) and RPA2 (**F**) foci in 786-O *PBRM1*-isogenic cells exposed to increasing concentrations of olaparib (µM) or DMSO (vehicle) for 48 hr. A minimum of 250 nuclei per condition were analyzed. Box-and-whisker plots show the number of foci per nucleus. Boxes indicate median, lower and upper quartiles; whiskers indicate

the 5th to 95th percentile range; outliers are shown as single data points; two-way ANOVA and *post hoc* Sidak's test. Data from one representative biological replicate of three independent experiments are shown. **G,** Schematic representation of the DNA fiber combing assay evaluating replication fork speed. **H**, **I**, Assessment of replication fork speed (kb/min) in 786-O (**H**) and U2OS (**I**) *PBRM1*-isogenic cells. A minimum of 500 forks per condition were analyzed. Mean ± SD, each dot represents a single replication fork; *n* = 2, Wilcoxon-Mann-Whitney test. **J,** Western blot of ATM, ATR, CHK1, and their corresponding phosphorylated forms in synchronized 786-O *PBRM1*-isogenic cells exposed to 20 µM olaparib for 48 hr, with and without subsequent drug removal for 72 hr; NT, untreated; V, DMSO vehicle; Ola, olaparib. **K, L,** Scatter plots showing the percentage of micronuclei-positive cells after 48 hr exposure to DMSO (vehicle), 0.5 µM mitomycin C (positive control), 1 µM olaparib or 200 nM talazoparib in 786-O (**K**) and U2OS (**L**) *PBRM1*-isogenic cells. Three independent fields with > 500 nuclei were analyzed. Mean ± SD, *n* = 3; two-way ANOVA and *post hoc* Sidak's test. Representative immunofluorescence images of a 786-O *PBRM1*-KO micronuclei-positive cell are shown in **K**. Scale bar: 20 µm.

Figure 4. PBRM1 deficiency associates with increased R-loop burden. A, RNA:DNA hybrid dot blot of genomic DNA extracted from 786-O *PBRM1*-isogenic cells in the presence and absence of RNase H digestion. S9.6 antibody was used to detect RNA:DNA hybrids with dsDNA antibody as a loading control. Serial dilutions of genomic DNA (1:1 = 2 µg) were probed with S9.6 antibody for standards (right panel). **B,** Bar plot showing S9.6 / dsDNA signal intensity normalized to the *PBRM1*-WT condition. Mean ± SD, *n* = 3; Welch's t-test. **C**, First, second and third component analysis (PCA) of the 786-O DRIP-Seq dataset, with the percentage of total variance explained by each component. For each 786-O replicate, normalized read counts of all binding sites were examined. **D**, Representative IGV (Integrative Genomics Viewer) tracks of genomic loci with DRIP-Seq peaks in 786-O *PBRM1*-isogenic cell lines, in the presence or absence of talazoparib; input and RNase H treatment are shown as negative controls. **E, F,** Bar plots displaying the baseline number of genomic loci with DRIP-Seq peaks in merged replicates of 786-

O **(E)** or H1299 **(F)** *PBRM1*-isogenic cells. Connected or overlapping peaks are counted as the minimal number of peaks involved in any group. **G**, UpSet plots showing the baseline number of genomic loci with DRIP-Seq peaks in 786-O *PBRM1*-isogenic cells, according to their genomic localization. Peaks overlapping with more than one feature are indicated by connected dots below the graph. Horizontal bars on the bottom right indicate the total number of genomic loci of each feature. Stacked pie charts provide an additional representation of the genomic repartition of DRIP-Seq peaks. Both replicates were merged for the analysis. **H**, Mirror bar chart displaying the number of consensus peaks significantly enriched in the first condition (Condition 1) compared to the second condition (Condition 2) in the 786-O *PBRM1*-isogenic model, after differential analysis using DESeq2, FDR ≤ 0.05. A schematic of the quantitative analysis performed on consensus peaks (defined as peaks present at a given genomic loci in at least two samples of the whole dataset) is shown to the left. **I,** Western blot of V5-tagged RNase H1 exogenous expression in total cell extracts of H1299 *PBRM1*-isogenic cells subjected to stable RNase H1 overexpression. **J,** Dose-response survival curves of H1299 *PBRM1*-isogenic cells exposed to increasing concentrations of talazoparib for 6 days (short-term survival assay) in the presence or absence of RNase H1 overexpression. Mean ± SD, *n* = 3; two-way ANOVA. **K**, Bar plot displaying the clonogenic surviving fraction of U2OS *PBRM1*-isogenic cells exposed to 0.2 µM olaparib for 10 days, in the presence or absence of 0.1 µM 5,6-Dichlorobenzimidazole 1-β-D-ribofuranoside (DRB). Mean ± SD, *n* = 3; two-way ANOVA and *post hoc* Tukey's test.

Figure 5. PARP and ATR inhibitors induce a cGAS/STING-mediated tumor cell-autonomous immune response in PBRM1-deficient cells. **A**, Representative immunofluorescence images of DMSO-, olaparib-, and VE-822-treated H1299 *PBRM1*-isogenic cells. Cells were exposed to 20 µM olaparib, 500 nM VE-822, or DMSO (vehicle) for 72 hr. Micronuclei are indicated with arrows. Scale bar: 20 µm. **B**, **C**, Automated quantification of micronuclei in H1299 (**B**) or 786-O (**C**) *PBRM1*-isogenic cells exposed to increasing concentrations of olaparib (µM) and VE-822 (nM). Shown is the number of micronuclei per cell normalized to the *PBRM1*-WT DMSO condition. Mean

± SD, *n* = 3, Kruskal-Wallis test and *post hoc* Dunn's test, relative to *PBRM1*-WT DMSO control. **D**, Western blot of pTBK1 and pIRF3 in H1299 *PBRM1*-isogenic cells upon PARPi or ATRi exposure. Cells were exposed for 48 hr to DMSO (vehicle), or a dose range of olaparib or VE-822. **E**, **F**, RT-qPCR analysis of RNA isolated from H1299 *PBRM1*-isogenic cells upon exposure to VE-822, in the presence or absence of cGAS/STING silencing by siRNA. Cells were transfected with siCTRL or si*CGAS* + si*STING* and treated for 72 hr with DMSO or a dose range of VE-822 (nM). *CCL5* (**E**) and *CXCL10* (**F**) mRNA were analyzed separately relative to *GAPDH*. Box-and-whisker plots show arbitrary units of gene expression, normalized to the *PBRM1*-WT DMSO condition. Boxes indicate median and lower and upper quartiles; whiskers indicate the 5^{th} to 95^{th} percentile range; *n* = 4, Kruskal-Wallis test and post hoc Dunn's test, relative to the *PBRM1*-WT DMSO condition.

Figure 6. Model of PBRM1/DNA repair inhibitors synthetic lethality. **A**, PBRM1-proficient cells have a functional DNA damage response and minimal R-loop levels. **B**, Loss of *PBRM1* gene function impairs the DNA damage response, and leads to higher pre-existing levels of γH2AX foci and micronuclei, enhanced replication stress and increased R-loop burden. **C**, Exposure to PARPi or ATRi causes additional DNA damage and exacerbates the accumulation of micronuclei, which, in turn, activates the cGAS/STING innate immune signaling cascade and results in the cell-autonomous secretion of type I interferon chemokines. Eventually, prolonged exposure to PARPi or ATRi results in decreased survival of PBRM1-defective tumor cells through synthetic lethality.

Figure 1

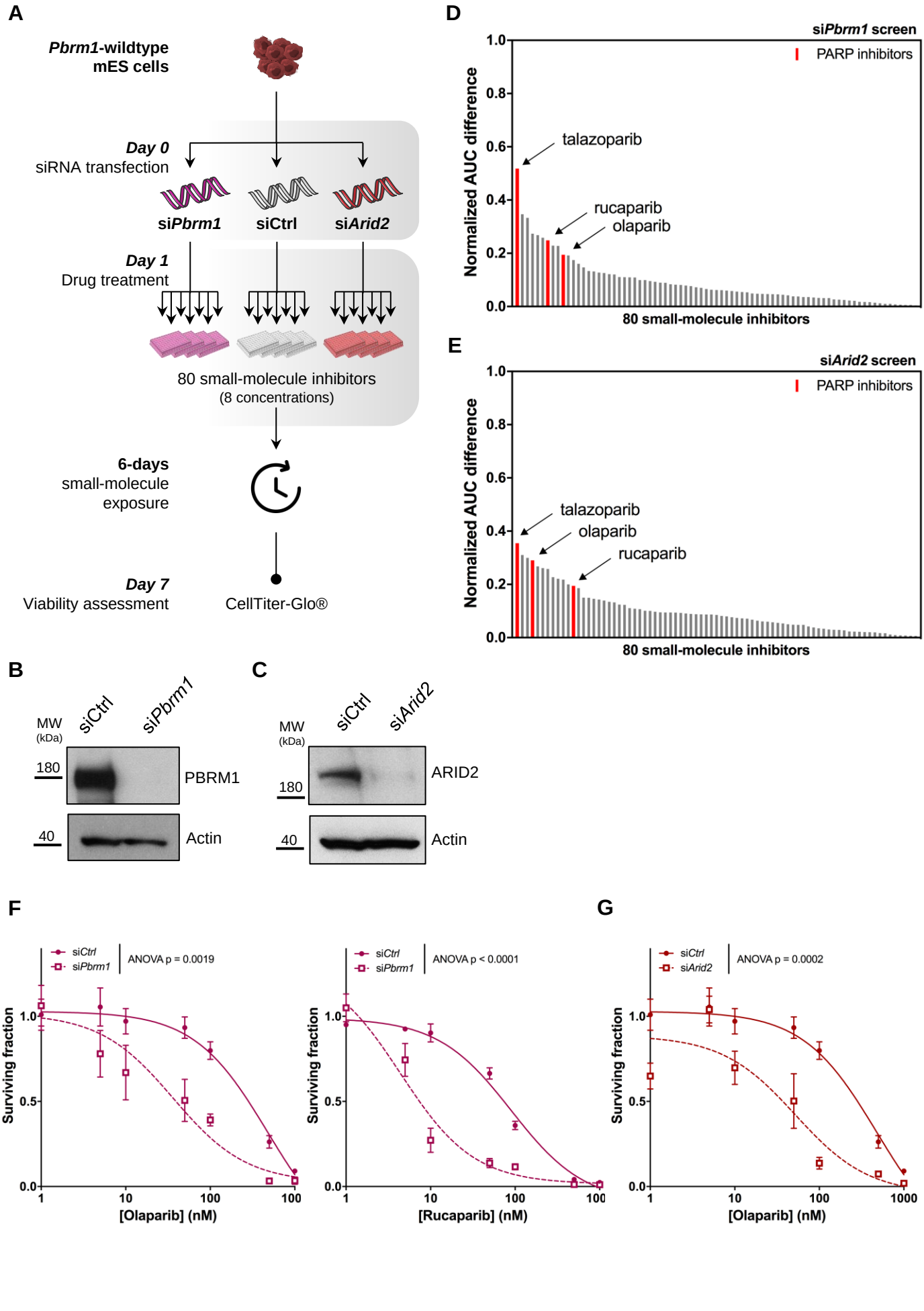
A
Pbrm1-wildtype mES cells
Day 0
siRNA transfection
siPbrm1
siCtrl
siArid2
Day 1
Drug treatment
80 small-molecule inhibitors
(8 concentrations)
6-days
small-molecule
exposure
Day 7
Viability assessment
CellTiter-Glo®
D
siPbrm1 screen
PARP inhibitors
Normalized AUC difference
talazoparib
rucaparib
olaparib
80 small-molecule inhibitors
E
siArid2 screen
PARP inhibitors
Normalized AUC difference
talazoparib
olaparib
rucaparib
80 small-molecule inhibitors
B
MW (kDa)
siCtrl
siPbrm1
180
PBRM1
40
Actin
C
MW (kDa)
siCtrl
siArid2
180
ARID2
40
Actin
F
siCtrl
siPbrm1
ANOVA p = 0.0019
Surviving fraction
[Olaparib] (nM)
siCtrl
siPbrm1
ANOVA p < 0.0001
Surviving fraction
[Rucaparib] (nM)
G
siCtrl
siArid2
ANOVA p = 0.0002
Surviving fraction
[Olaparib] (nM)

Figure 2

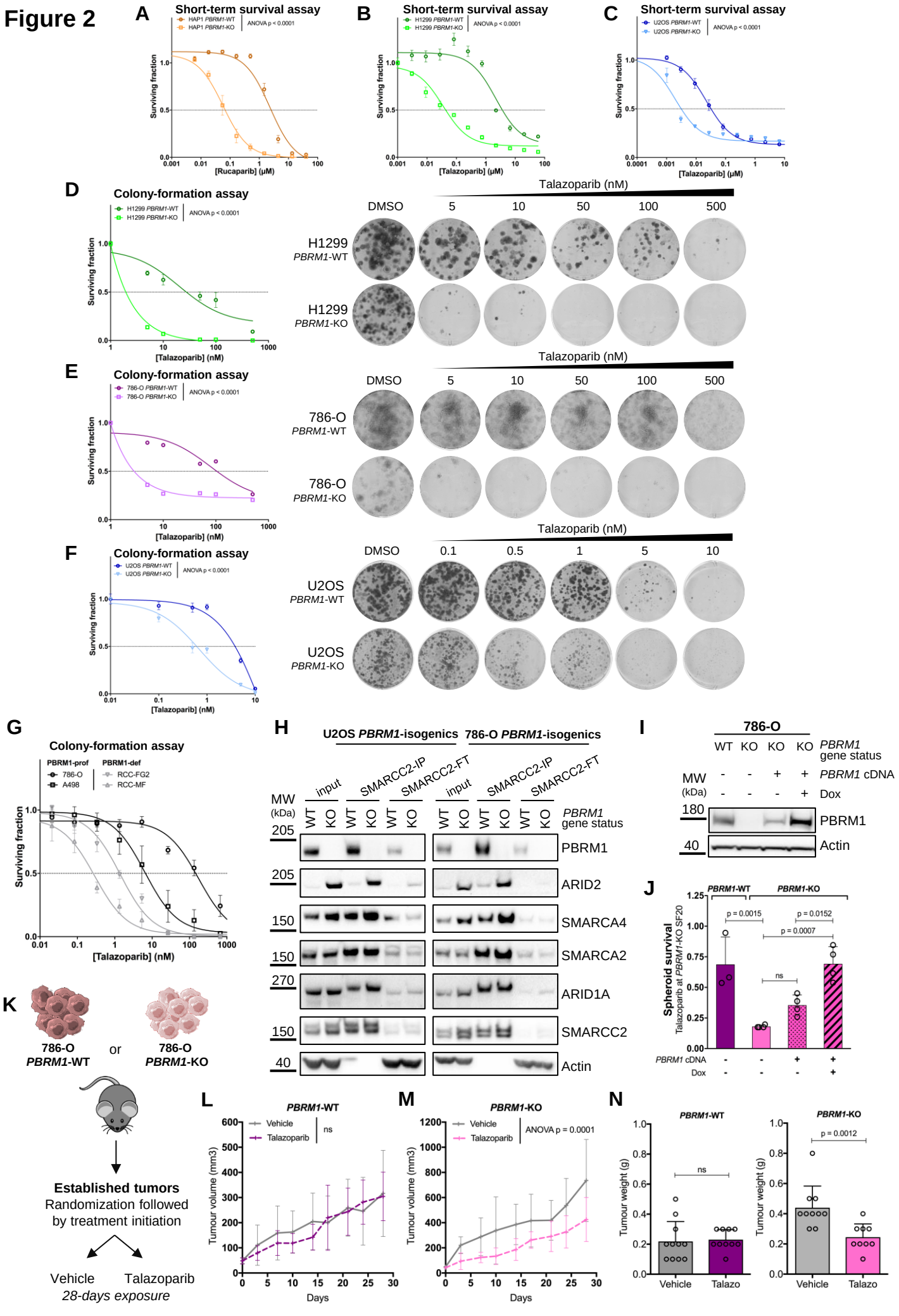
A
Short-term survival assay
HAP1 PBRM1-WT
HAP1 PBRM1-KO
ANOVA p < 0.0001
Surviving fraction
[Rucaparib] (μM)
B
Short-term survival assay
H1299 PBRM1-WT
H1299 PBRM1-KO
ANOVA p < 0.0001
Surviving fraction
[Talazoparib] (μM)
C
Short-term survival assay
U2OS PBRM1-WT
U2OS PBRM1-KO
ANOVA p < 0.0001
Surviving fraction
[Talazoparib] (μM)
D
Colony-formation assay
H1299 PBRM1-WT
H1299 PBRM1-KO
ANOVA p < 0.0001
Surviving fraction
[Talazoparib] (nM)
Talazoparib (nM)
DMSO
5
10
50
100
500
H1299 PBRM1-WT
H1299 PBRM1-KO
E
Colony-formation assay
786-O PBRM1-WT
786-O PBRM1-KO
ANOVA p < 0.0001
Surviving fraction
[Talazoparib] (nM)
Talazoparib (nM)
DMSO
5
10
50
100
500
786-O PBRM1-WT
786-O PBRM1-KO
F
Colony-formation assay
U2OS PBRM1-WT
U2OS PBRM1-KO
ANOVA p < 0.0001
Surviving fraction
[Talazoparib] (nM)
Talazoparib (nM)
DMSO
0.1
0.5
1
5
10
U2OS PBRM1-WT
U2OS PBRM1-KO
G
Colony-formation assay
PBRM1-prof
786-O
A498
PBRM1-def
RCC-FG2
RCC-MF
Surviving fraction
[Talazoparib] (nM)
H
U2OS PBRM1-isogenics
786-O PBRM1-isogenics
input
SMARCC2-IP
SMARCC2-FT
MW (kDa)
WT
KO
PBRM1 gene status
205
PBRM1
205
ARID2
150
SMARCA4
150
SMARCA2
270
ARID1A
150
SMARCC2
40
Actin
I
786-O
WT
KO
KO
KO
PBRM1 gene status
MW (kDa)
PBRM1 cDNA
Dox
180
PBRM1
40
Actin
J
PBRM1-WT
PBRM1-KO
Spheroid survival
Talazoparib at PBRM1-KO SF20
p = 0.0015
p = 0.0152
p = 0.0007
ns
PBRM1 cDNA
Dox
K
786-O PBRM1-WT
or
786-O PBRM1-KO
Established tumors
Randomization followed by treatment initiation
Vehicle
Talazoparib
28-days exposure
L
PBRM1-WT
Vehicle
Talazoparib
ns
Tumour volume (mm3)
Days
M
PBRM1-KO
Vehicle
Talazoparib
ANOVA p = 0.0001
Tumour volume (mm3)
Days
N
PBRM1-WT
ns
Tumour weight (g)
Vehicle
Talazo
PBRM1-KO
p = 0.0012
Tumour weight (g)
Vehicle
Talazo

Figure 3

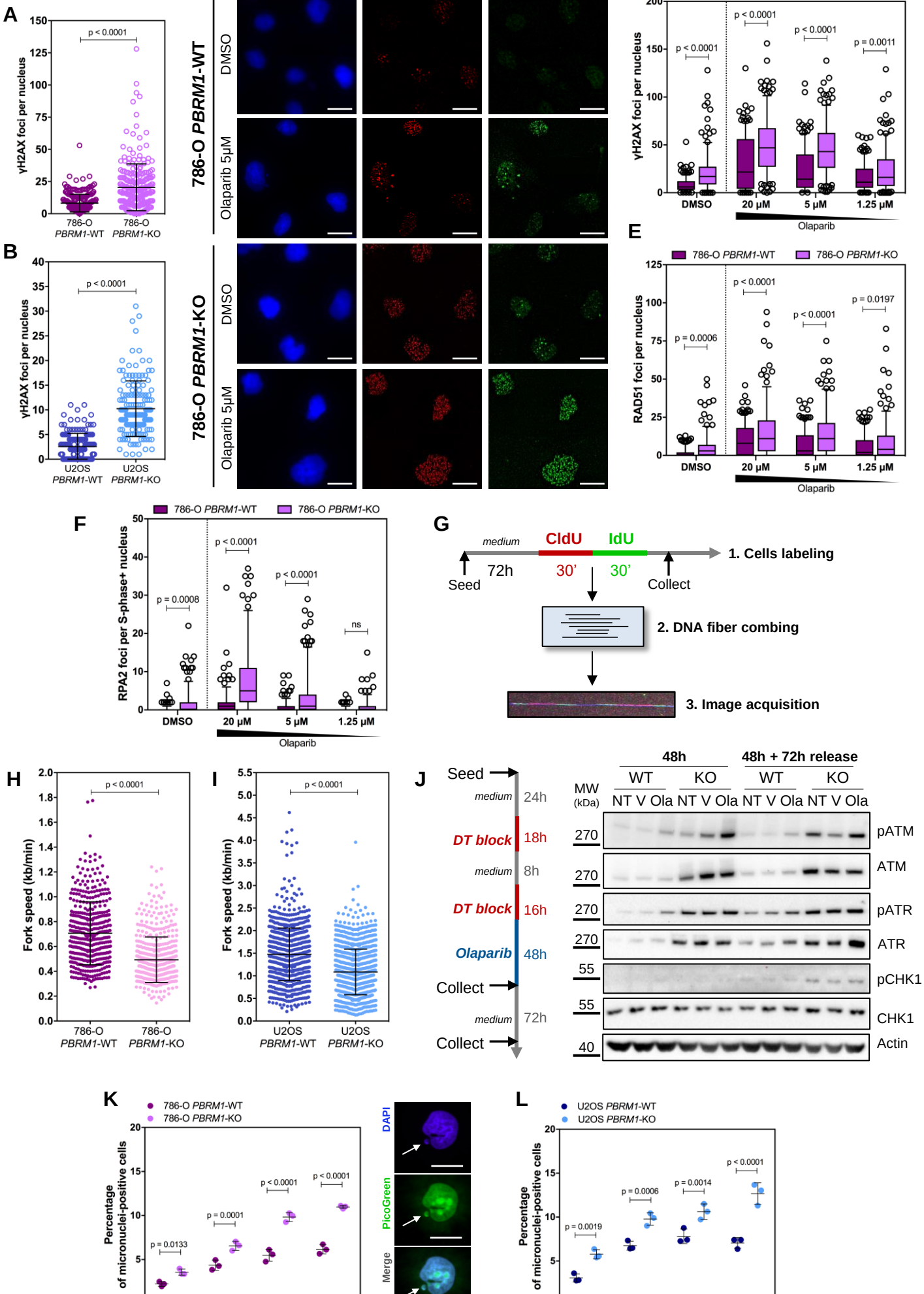
A
γH2AX foci per nucleus
p < 0.0001
786-O PBRM1-WT
786-O PBRM1-KO
B
γH2AX foci per nucleus
p < 0.0001
U2OS PBRM1-WT
U2OS PBRM1-KO
C
DAPI
γH2AX
RAD51
786-O PBRM1-WT
786-O PBRM1-KO
DMSO
Olaparib 5μM
D
786-O PBRM1-WT
786-O PBRM1-KO
γH2AX foci per nucleus
p < 0.0001
p < 0.0001
p < 0.0001
p = 0.0011
DMSO
20 μM
5 μM
1.25 μM
Olaparib
E
786-O PBRM1-WT
786-O PBRM1-KO
RAD51 foci per nucleus
p = 0.0006
p < 0.0001
p < 0.0001
p = 0.0197
DMSO
20 μM
5 μM
1.25 μM
Olaparib
F
786-O PBRM1-WT
786-O PBRM1-KO
RPA2 foci per S-phase+ nucleus
p = 0.0008
p < 0.0001
p < 0.0001
ns
DMSO
20 μM
5 μM
1.25 μM
Olaparib
G
medium
CldU
IdU
72h
30'
30'
Seed
Collect
1. Cells labeling
2. DNA fiber combing
3. Image acquisition
H
Fork speed (kb/min)
p < 0.0001
786-O PBRM1-WT
786-O PBRM1-KO
I
Fork speed (kb/min)
p < 0.0001
U2OS PBRM1-WT
U2OS PBRM1-KO
J
Seed
medium 24h
DT block 18h
medium 8h
DT block 16h
Olaparib 48h
Collect
medium 72h
Collect
48h
48h + 72h release
WT
KO
WT
KO
MW (kDa)
NT V Ola NT V Ola NT V Ola NT V Ola
270 pATM
270 ATM
270 pATR
270 ATR
55 pCHK1
55 CHK1
40 Actin
K
786-O PBRM1-WT
786-O PBRM1-KO
Percentage of micronuclei-positive cells
p = 0.0133
p = 0.0001
p < 0.0001
p < 0.0001
DMSO
MMC
Olaparib
Talazoparib
DAPI
PicoGreen
Merge
L
U2OS PBRM1-WT
U2OS PBRM1-KO
Percentage of micronuclei-positive cells
p = 0.0019
p = 0.0006
p = 0.0014
p < 0.0001
DMSO
MMC
Olaparib
Talazoparib

Figure 4

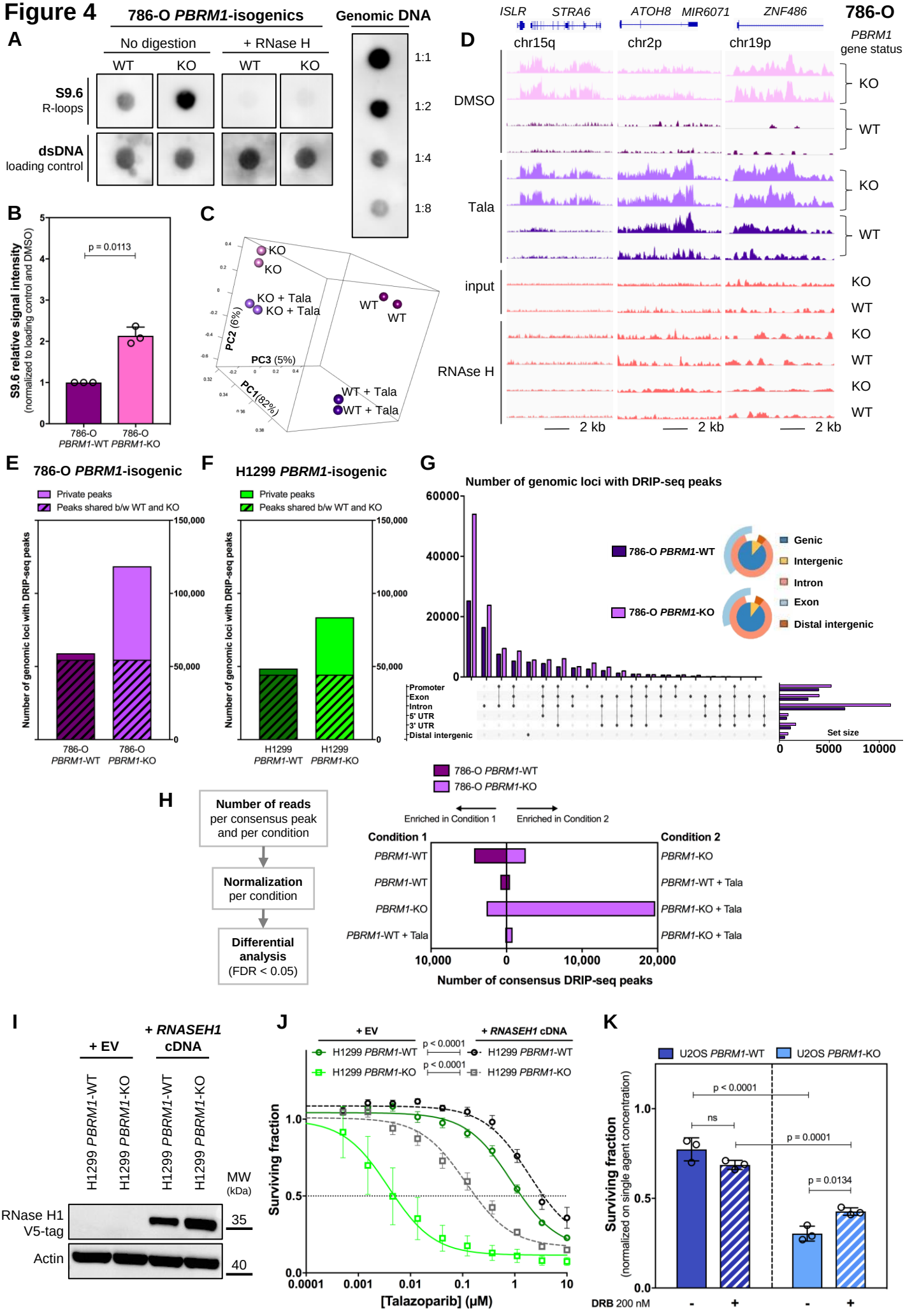
A
786-O PBRM1-isogenics
Genomic DNA
No digestion
+ RNase H
WT
KO
WT
KO
S9.6
R-loops
dsDNA
loading control
1:1
1:2
1:4
1:8
B
S9.6 relative signal intensity
(normalized to loading control and DMSO)
p = 0.0113
786-O PBRM1-WT
786-O PBRM1-KO
C
KO
KO
KO + Tala
KO + Tala
WT
WT
WT + Tala
WT + Tala
PC2 (6%)
PC3 (5%)
PC1(82%)
D
ISLR
STRA6
ATOH8
MIR6071
ZNF486
786-O
PBRM1 gene status
chr15q
chr2p
chr19p
DMSO
Tala
input
RNAse H
KO
WT
2 kb
E
786-O PBRM1-isogenic
Private peaks
Peaks shared b/w WT and KO
Number of genomic loci with DRIP-seq peaks
150,000
100,000
50,000
0
786-O PBRM1-WT
786-O PBRM1-KO
F
H1299 PBRM1-isogenic
Private peaks
Peaks shared b/w WT and KO
H1299 PBRM1-WT
H1299 PBRM1-KO
G
Number of genomic loci with DRIP-seq peaks
60000
40000
20000
0
786-O PBRM1-WT
786-O PBRM1-KO
Genic
Intergenic
Intron
Exon
Distal intergenic
Promoter
Exon
Intron
5' UTR
3' UTR
Distal intergenic
Set size
0
5000
10000
H
Number of reads
per consensus peak
and per condition
Normalization
per condition
Differential
analysis
(FDR < 0.05)
786-O PBRM1-WT
786-O PBRM1-KO
Enriched in Condition 1
Enriched in Condition 2
Condition 1
Condition 2
PBRM1-WT
PBRM1-KO
PBRM1-WT
PBRM1-WT + Tala
PBRM1-KO
PBRM1-KO + Tala
PBRM1-WT + Tala
PBRM1-KO + Tala
10,000
0
10,000
20,000
Number of consensus DRIP-seq peaks
I
+ EV
+ RNASEH1 cDNA
H1299 PBRM1-WT
H1299 PBRM1-KO
H1299 PBRM1-WT
H1299 PBRM1-KO
MW (kDa)
RNase H1 V5-tag
35
Actin
40
J
+ EV
+ RNASEH1 cDNA
H1299 PBRM1-WT
H1299 PBRM1-KO
p < 0.0001
p < 0.0001
H1299 PBRM1-WT
H1299 PBRM1-KO
Surviving fraction
1.0
0.5
0.0
0.0001
0.001
0.01
0.1
1
10
[Talazoparib] (μM)
K
U2OS PBRM1-WT
U2OS PBRM1-KO
p < 0.0001
ns
p = 0.0001
p = 0.0134
Surviving fraction
(normalized on single agent concentration)
1.0
0.5
0.0
DRB 200 nM
-
+
-
+

Figure 5

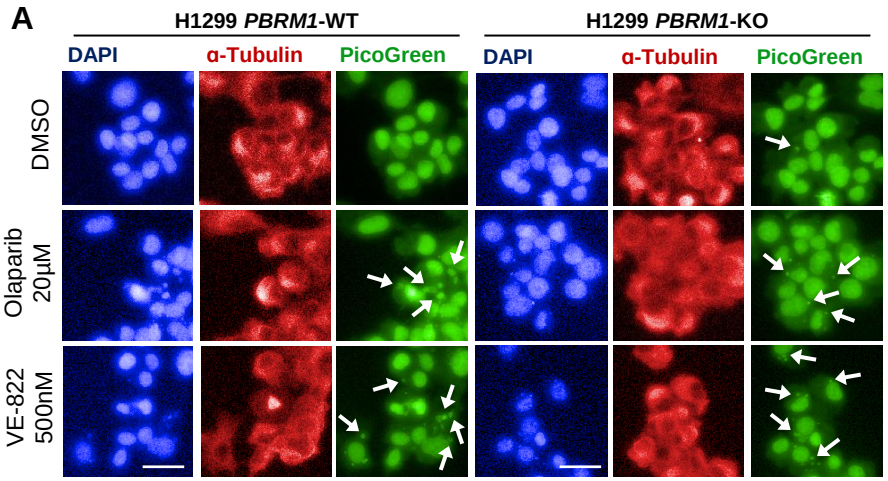
A
H1299 PBRM1-WT
H1299 PBRM1-KO
DAPI
α-Tubulin
PicoGreen
DMSO
Olaparib 20μM
VE-822 500nM

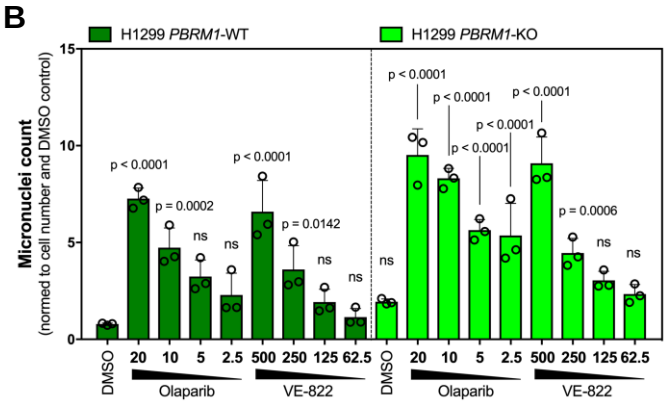
B
H1299 PBRM1-WT
H1299 PBRM1-KO
Micronuclei count
(normed to cell number and DMSO control)
DMSO
Olaparib
VE-822

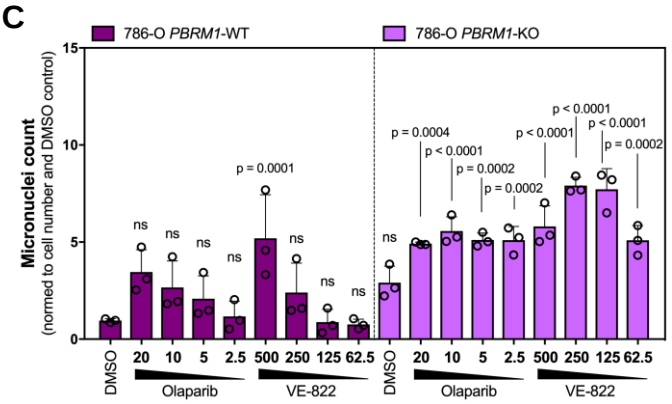
C
786-O PBRM1-WT
786-O PBRM1-KO
Micronuclei count
(normed to cell number and DMSO control)
DMSO
Olaparib
VE-822

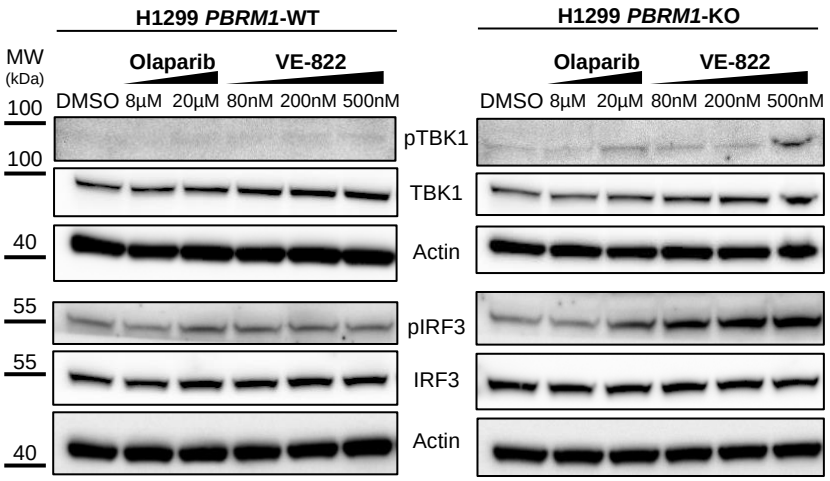
D
H1299 PBRM1-WT
H1299 PBRM1-KO
MW (kDa)
Olaparib
VE-822
DMSO 8μM 20μM 80nM 200nM 500nM
pTBK1
TBK1
Actin
pIRF3
IRF3
Actin

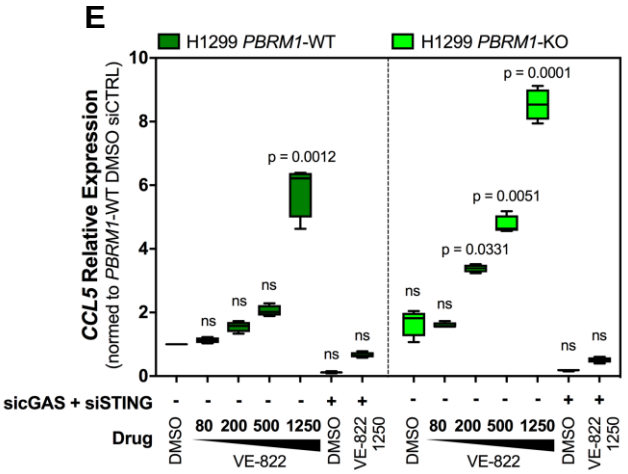
E
H1299 PBRM1-WT
H1299 PBRM1-KO
CCL5 Relative Expression
(normed to PBRM1-WT DMSO siCTRL)
siCGAS + siSTING
Drug
VE-822

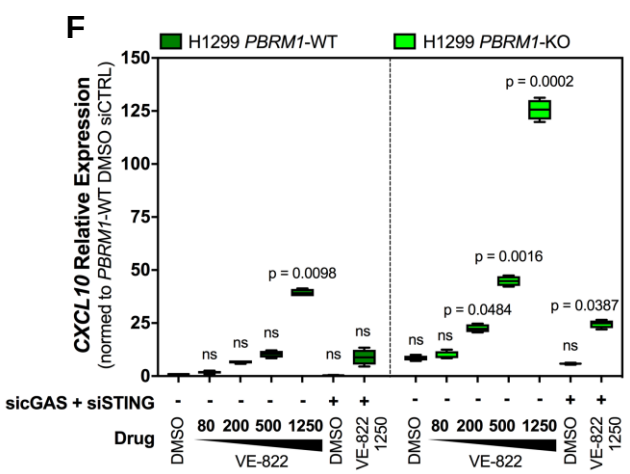
F
H1299 PBRM1-WT
H1299 PBRM1-KO
CXCL10 Relative Expression
(normed to PBRM1-WT DMSO siCTRL)
siCGAS + siSTING
Drug
VE-822

Figure 6

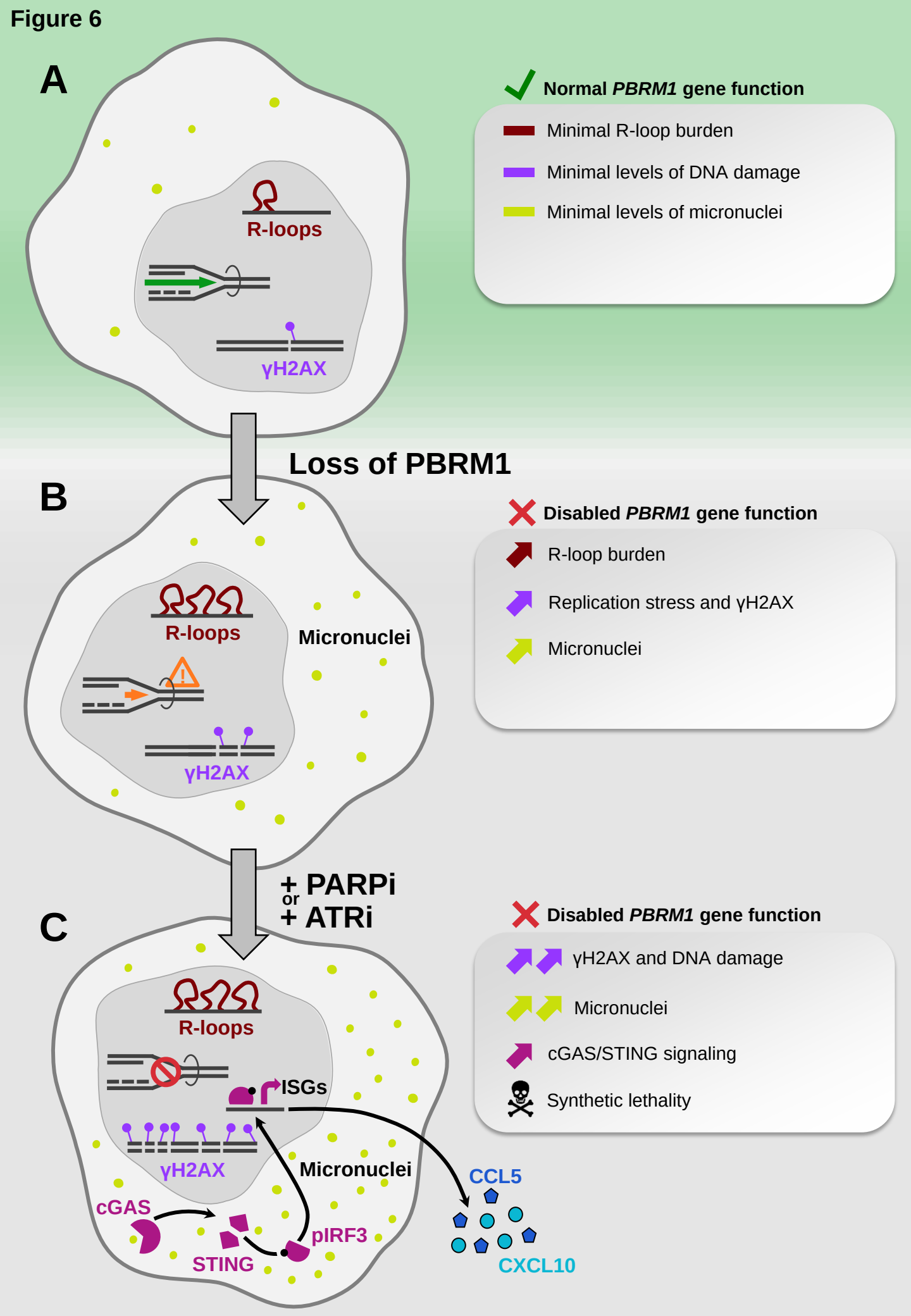
A
R-loops
γH2AX
Normal PBRM1 gene function
Minimal R-loop burden
Minimal levels of DNA damage
Minimal levels of micronuclei
Loss of PBRM1
B
R-loops
Micronuclei
γH2AX
Disabled PBRM1 gene function
R-loop burden
Replication stress and γH2AX
Micronuclei
+ PARPi
or
+ ATRi
C
R-loops
ISGs
γH2AX
Micronuclei
cGAS
STING
pIRF3
CCL5
CXCL10
Disabled PBRM1 gene function
γH2AX and DNA damage
Micronuclei
cGAS/STING signaling
Synthetic lethality